adult mice generated characteristic large EEG spikes and that pharmacological blockade of CA3 NMDA receptors enhanced the susceptibility to kainate-induced seizures. These results raise an intriguing possibility that NMDA receptors may control negatively the excitability of the hippocampal CA3 recurrent network as a whole *in vivo*.

Methods

Generation of mice

Genomic DNA carrying the exon 11 to 22 of the *GluRζ1* gene was isolated by screening a bacterial artificial chromosome (BAC) library prepared from the C57BL/6 strain (Incyte Genomics) with the 2.2 kb-*Eco*RI fragment from pBKSAζ1 [16]. The 13.3-kb *Eco*RI-*Xba*I fragment of the BAC clone was used for construction of the targeting vector. The *loxP* site was inserted into the *Bam*HI site between exon 18 and 19, and the 1.8-kb DNA fragment carrying the *loxP* sequence and *Pgk-1* promoter-driven neomycin phosphotransferase gene (*neo*) flanked by two Flp recognition target (*frt*) sites into the *Spe*I site between exon 20 and 21. Endogenous *Eco*RI site at the 5′ end of 13.3-kb *Eco*RI-*Xba*I genomic fragment was replaced with *Not*I site and an exogenous *Eco*RI site was inserted between the second *loxP* site and *neo* gene. The targeting vector pζ1TV was composed of the 14.8-kb *Not*I-*Xba*I fragment, MC1 promoter-driven diphteria toxin gene derived from pMC1DTpA and pBluescript II SK(+) [17]. The targeting vector was linearized by *Not*I and electroporated into ES cells derived from the C57BL/6N strain [18,19]. Recombinant clones were identified by Southern blot analysis of *Eco*RI-digested genomic DNA using 284-bp fragment amplified with primers 5′-ATAGAGAAAGACATGGGGC-3′ and 5′-TGCTACTGTGCAGGAAGTG-3′ from pζ1TV, the 0.6 kb *Pst*I fragment from pLFNeo [20], and the 1.1-kb *Xho*I–*Eco*RI fragment from the BAC clone as 5′ inner, neo, and 3′ outer probes, respectively. The $GluR\zeta1^{flox}$ allele was also identified by PCR using primers 5′-GCAGTGAGGCTCACACAGGCCTGAAGACTA-3′ and 5′-AGTGAACTCGGATCCTGACCATTGGCCACT-3′. Chimeric mice production and elimination of the *neo* gene from the genome through Flp/frt-mediated excision were carried out essentially as described [18–20].

GluRγ1-Cre mice were obtained by inserting the *cre* gene in the translational initiation site of the *GluRγ1* gene in frame using ES cells derived from the C57BL/6N strain [19]. The 1.8-kb DNA fragment, which carried the polyadenylation signal sequence and *pgk-1* promoter-driven *neo* gene flanked by two *frt* sites [20], was inserted into the downstream of the *cre* gene. $GluR\zeta1^{+/flox}$ mice were crossed with GluRγ1-Cre mice to yield $GluR\gamma1^{+/cre}$; $GluR\zeta1^{flox/flox}$ mice. The $GluR\gamma1^{+/cre}$ allele was identified by PCR using primers 5′-AACTGCAGTCTTGCATGCTCTCTGGAGCC-3′, 5′-GGAGCGGAGACACGGGGCAT-3′ and 5′-TTGCCCCTGTTTCACTATCC-3′. Cre recombinase-mediated NMDA receptor ablation is hippocampal CA3 pyramidal neuron-specific in $GluR\gamma1^{+/cre}$; $GluR\zeta1^{flox/flox}$ mice (Fig. 1). It is unknown why the *GluRγ1* promoter-driven Cre expression does not exactly follow the expression pattern of GluRγ1 [21]. The insertion of the *pgk-1* promoter-driven *neo* gene and the polyadenylation signal sequence together may affect the Cre expression pattern since the elimination of the *neo* gene through Flp-mediated recombination altered the expression pattern.

All animal procedures were approved by the Animal Care and the Use Committee of Graduate School of Medicine, the University of Tokyo (Approval # 1721T062). Mice were fed *ad libitum* with standard laboratory chow and water in standard animal cages under a 12 h light/dark cycle.

AAV-Cre vector

We employed AAV to deliver Cre recombinase since AAV is safe, non-pathogenic, non-inflammatory and extremely stable stable [22,23]. AAV-Cre or AAV-EGFP vector contains an expression cassette consisting of a human cytomegalovirus immediate-early promoter (CMV promoter), followed by the human growth hormone first intron, cDNA of Cre recombinase with a nuclear localization signal or the enhanced green fluorescence protein (EGFP), and simian virus 40 polyadenylation signal sequence (SV40 polyA), between the inverted terminal repeats (ITR) of the AAV-2 genome. The two helper plasmids, pAAV-RC and pHelper (Agilent Technologies, Santa Clara, California), harbor the AAV *rep* and *cap* genes, and the *E2A*, *E4*, and *VA RNA* genes of the adenovirus genome, respectively. HEK293 cells were cotransfected by the calcium phosphate coprecipitation method with the vector plasmid, pAAV-RC, and pHelper. AAV vectors were then harvested and purified by two sequential continuous iodoxale ultracentrifugations. The vector titer was determined by quantitative DNA dot-blot hybridization or quantitative PCR of DNase-I-treated vector stocks. Before administration, AAV vectors were diluted in phosphate-buffered saline to $5–8\times10^{10}$ genome copies/μl. A glass micropipette was inserted into the hippocampal CA3 region of ketamine-anesthetized mice (AP, L, V = −1.2, ±1.2, +2.0; −1.7, ±2.0, +2.1; −2.2, ±2.5, +2.4; −2.7, ±3.2, +3.5; −3.2, ±2.5, +4.0). Two minutes after the insertion, 1.0 μl of a virus solution or vehicle was injected at a constant flow rate of 16.6 nl/min, and the glass micropipette was left in this configuration for an additional 2 min, to prevent reflux of the injected material along the injection track, before being slowly retracted. AAV spread 0.5–0.7 mm both rostrodorsally and laterally. For every injected animal, the limit of the infected region was verified by immunohistochemistry for Cre recombinase or GluRζ1.

Immunological analysis

Immunohistochemistry was done as described [24] using antibodies against VGluT2 (guinea pig) [25], Calbindin (rabbit) [26], PSD-95 (rabbit) [27], GluRα1 (rabbit) [28], GAD (guinea pig) [29], and Cre recombinase (1:1000; rabbit; Novagen). Immunobloting analyses in whole-brain homogenate were carried out using antibodies for GluRζ1 (rabbit) [30], and neuron-specific enolase (1:4000; Chemicon) and chemiluminescense (Amersham Biosciences).

Golgi staining

Coronal brain sections (2 mm) were immersed for 4 days in a solution composed of 5% glutaraldehyde (Wako) and 2% $K_2Cr_2O_7$ (Sigma) and then transferred to a 0.75% solution of $AgNO_3$ (Sigma) for further 4 days. The treated brain was sectioned (100 μm), dehydrated and mounted on glass slides.

Morphology of AAV-EGFP infected CA3 neurons

AAV-EGFP vector was delivered into the hippocampal CA3 region of ketamine-anesthetized control and mutant mice of 8 weeks old. Fourteen days later, fixed coronal brain sections (150 μm) were prepared. Neurons were examined with a Leica SP-5 confocal laser scanning microscope. Optical sections were collected at intervals of 0.15 μm and averaged 16 times using a 100×objective (N.A. 1.4). The distance between axonal varicosities was measured from 50 μm-portions of CA3 axons within the CA3 stratum radiatum [31]. For spine analysis, only spines on clearly visible tertiary apical and basal branches were imaged. During the quantitation of the spine density, putative spines in the

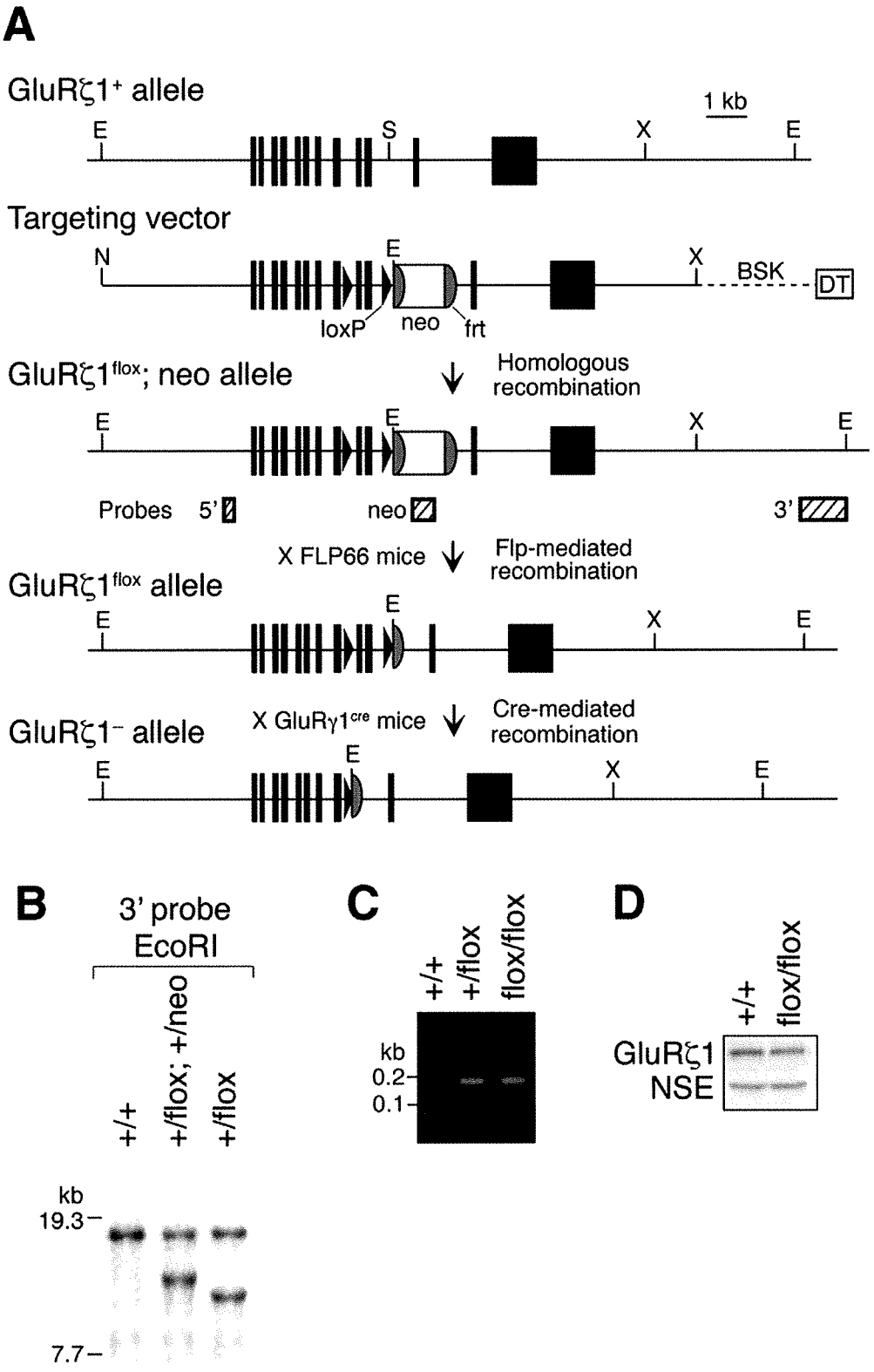
A
GluRζ1+ allele
1 kb
E
S
X
E
Targeting vector
N
E
X
BSK
DT
loxP
neo
frt
GluRζ1flox; neo allele
Homologous recombination
E
E
X
E
Probes 5'
neo
3'
X FLP66 mice
Flp-mediated recombination
GluRζ1flox allele
E
X
E
GluRζ1− allele
X GluRγ1cre mice
Cre-mediated recombination
E
X
E
B
3' probe EcoRI
+/+
+/flox; +/neo
+/flox
kb
19.3
7.7
C
+/+
+/flox
flox/flox
kb
0.2
0.1
D
+/+
flox/flox
GluRζ1
NSE

Figure 1. Generation of *GluRζ1*^{flox} mice by homologous recombination in C57BL/6 strain derived ES cells. A, Schema of the exons 11–22 region of the *GluRζ1* gene (*GluRζ1*$^{+}$), targeting vector, floxed and *neo*-inserted allele (*GluRζ1*^{flox}; *neo*), and floxed allele (*GluRζ1*^{flox}). Exons 19 and 20 encode the putative transmembrane segment M4 of GluRζ1. The *GluRζ1*^{flox}; *neo* allele contains two *loxP* sequences flanking exons 19 and 20 of the *GluRζ1* gene and the *neo* gene flanked by two *frt* sequences. The *neo* gene was removed *in vivo* by crossing *GluRζ1*$^{+/flox}$; +/*neo* mice with FLP66 mice carrying the Flp recombinase gene under the control of the *EF1α* promoter. *GluRζ1*$^{+/flox}$ mice were crossed with GluRγ1-Cre mice to disrupt the GluRζ1 gene selectively in the hippocampal CA3 region. Abbreviations: BSK, plasmid pBluescript; DT, diphtheria toxin gene; neo, neomycin phosphotransferase gene; E, *Eco*RI; N, *Not*I; S, *Spe*I; X, *Xba*I. Hatched boxes indicate the location of probes for Southern blot analysis. **B**, Southern blot analysis of genomic DNA from *GluRζ1*$^{+/+}$, *GluRζ1*$^{+/flox}$; +/*neo*, and *GluRζ1*$^{+/flox}$ mice. *Eco*RI-digested DNA was hybridized with 3′ probe. **C**, Agarose gel electrophoresis of DNA fragments amplified by PCR from *GluRζ1*$^{+/+}$, *GluRζ1*$^{+/flox}$ and *GluRζ1*$^{flox/flox}$ mice. The amplified DNA fragments derived from the *GluRζ1*$^{+}$ and *GluRζ1*^{flox} alleles were 61 bp and 169 bp, respectively. **D**, Western blot analysis of GluRζ1 and neuron-specific enolase (NSE) proteins in whole-brain homogenates from *GluRζ1*$^{+/+}$ and *GluRζ1*$^{flox/flox}$ mice.
doi:10.1371/journal.pone.0003993.g001

three-dimensional reconstructed image were compared with both the unprocessed, individual optical sections and with a 'movie', in which segments of the three-dimensional reconstruction were rotated around the dendritic axis (IMARIS, Bitplane). For dendritic analysis, neurons were imaged on a Leica SP-5 with a 40×objective (N.A. 0.8). Optical sections were collected at intervals of 2 μm and averaged 8 times. The topographical order of the dendritic tree was made using the semi-automated program FilamentTracer (Bitplane). Analysis of dendritic topology included dendritic branches up to the third order. Analysis of dendritic spines was performed in rather linear, apical secondary and tertiary dendrites.

In situ hybridization

Isotopic detection of mRNAs was performed as described [32]. All samples were subjected to hybridization analysis at the same time and sections were exposed to a single x-ray film for measurement of relative optical density with IP Lab software. The relative expression levels of the mRNAs in the hippocampal CA3 region were calculated using the ratio of the density in the CA3 region to that of the CA1 region, except that the *GluRγ1* mRNA density in the CA3 region was directly compared between control and mutant mice. Double *in situ* hybridization was performed with mixture of [^{33}P]dATP-labeled oligonucleotide probe for GluRζ1 (complementary to residues 2583–2627, GenBank accession No. D10028) and digoxigenin (DIG)-labeled cRNA probe for GAD67 (complementary to residues 802–1617, No. A28072) as described [33]. Hybridization signals were visualized with nuclear track emulsion (NTB-2, Kodak) and fluorescent substrate (HNPP Fluorescent Detection Set, Boehringer-Mannheim), respectively. Sections were counterstained with NeuroTrace 500/525 green (Molecular Probes).

Kainate-induced seizure

Kainate was intraperitoneally administered to mice, and they were monitored for 1 h to determine whether they exhibited seizures with generalized tonic-clonic activity accompanying the loss of postural tone. Mice were then fixed under deep pentobarbital anesthesia for immunohistochemical analysis with the c-Fos antibody (Oncogene) 2 h after kainate administration.

Electrophysiology

Transverse hippocampal slices (400 μm thick) were superfused with an artificial cerebrospinal fluid (aCSF) containing (in mM): 119 NaCl, 2.5 KCl, 2.5 $CaCl_2$, 1.3 $MgSO_4$, 1 NaH_2PO_4, 26.2 $NaHCO_3$, and 11 glucose, which was equilibrated with 95% O_2/5% CO_2. Synaptic responses were evoked via a bipolar stimulating electrode placed in the CA3 stratum radiatum and whole-cell recordings were made from CA3 pyramidal cells using the blind-patch technique. The stimulus strength was set at the beginning of each experiment so that the average amplitude of synaptic responses in the absence of any antagonists is around 200 pA at a holding potential of −80 mV. The AMPA receptor-mediated excitatory postsynaptic current (AMPA-EPSC) was isolated by subtracting the synaptic response in the presence of 10 μM 6-cyano-7-nitroquinoxaline-2,3-dione (CNQX) from that in its absence. The NMDA receptor-mediated excitatory postsynaptic current (NMDA-EPSC) was recorded at +50 mV in the presence of 10 μM CNQX and 0.1 mM picrotoxin. The $GABA_A$ receptor-mediated inhibitory postsynaptic current ($GABA_A$-IPSC) was recorded at 0 mV in the presence of 10 μM CNQX and 25 μM D-2-amino-5-phosphonovaleric acid (D-APV). The stimulus strength was constant throughout each experiment. The slow hyperpolarizing currents induced by high-frequency stimulation (50 Hz, 40 pulses) were recorded at −20 mV in the presence of 0.1 mM picrotoxin as described previously [34]. Patch electrodes were filled with an internal solution containing (in mM): 140 potassium methansulfonate, 8 NaCl, 10 HEPES, 2 MgATP, and 0.3 Na_3-GTP (pH 7.2 adjusted with KOH, osmolarity 290 to 300 mOsm). For pharmacological experiments, 10 mM BAPTA was added in the pipette solution or potassium methansulfonate in the pipette solution was replaced by cesium methansulfonate. Voltage-clamped responses were recorded with an Axopatch 1D amplifier (Axon Instruments, Union City, CA, USA) and the signal was filtered at 1 kHz, digitized at 2.5 kHz, and stored on a personal computer.

Field potential recording *in vivo*

Urethane-anesthetized mice (1 g/kg body weight, i.p.) were fixed in a stereotaxic head holder (Narishige). For the recording of local field potentials, a tungsten electrode (2–5 MΩ, Frederick Haer) or a silicon probe (16 recoding sites with 50 μm separation, NeuroNexus Technologies) was inserted into the hippocampal CA3 region (AP = −2.0 mm from bregma, L = ±2.3 mm from midline, and V = +2.0 mm ventral to dura), the hippocampal CA1 region (AP = −2.0, L = ±1.0, V = +1.2) or the dentate gyrus (AP = −2.0, L = ±1.0, V = +2.0). Signals were amplified (MEG-1200, Nihon Kohden), band-pass filtered (0.08–1,000 Hz), digitized at 1 kHz through an AD converter (National Instruments), and stored in a computer. Analyses of data were performed offline using LabVIEW (National Instruments) and IGOR (Wave matics) software. Recordings using a glass electrode (10–15 MΩ, GD-2, Narishige) were carried out as described [35]. Raw traces (0.08–3,000 Hz) were band-pass filtered for the detection of MUA of neurons (0.15–3 kHz). EEG spikes with power of twice the s.d. from the baseline mean and the duration of about 30 ms were extracted. The unit activity was defined as a power of more than five times the s.d. from the baseline mean and the duration of less than 4 ms [7]. The locations of the electrode were verified histologically. CSD analyses were carried out as described [8].

Pharmacological experiments. Mice were anesthetized with ketamine (80 mg/kg, i.p.; Sankyo Co., Tokyo, Japan) and xylazine (20 mg/kg i.p.; Bayer, Tokyo, Japan), and fixed to a

stereotaxic apparatus (David Kopf, Tujunga, CA, USA). Two single guide cannulae (Plastics One, Roanoke, VA, USA) were implanted into the CA3 region of the hippocampus bilaterally (stereotaxic coordinates: AP = −2.2 mm from bregma, ML = ±2.5 mm from midline, DV = +1.4 mm from bregma), according to an atlas of the mouse brain [36]. The tip of the internal cannula for microinjection was inserted 1 mm below the tip of the guide cannulae (DV = +2.4 mm from bregma). The cannulae were fixed to the skull with dental cement. The animals were allowed to recover for at least 5 days. D,L-APV (Sigma-Aldrich, MO, USA) was dissolved in aCSF at a concentration of 30 mM. The aCSF was consisted of NaCl (150 mM), KCl (3 mM), $CaCl_2$ (1.4 mM), $MgCl_2$ (0.8 mM), Na_2HPO_4 (0.8 mM), and NaH_2PO_4 (0.2 mM). During drug infusions, the mice were restrained lightly in the disposable vinyl jacket (Braintree Scientific, Inc, MA, USA) and 0.5 µl of the drug or aCSF was infused at a rate of 0.2 µl/min using a microinjection pump (CMA/100, CMA/Microdialysis, Solna, Sweden). The infusion cannulae (bilateral) were left in place for a further 1 min to diffuse the drug from the needle tip, and the animal was then returned to its home cage. Kainate was delivered i.p. 20–30 min after APV injection.

Statistical analysis

All behavioral experiments were performed in a blind fashion. Data were expressed as mean±SEM. Statistical analysis was performed using Fisher's exact probability test, Kolmogorov-Smirnov test, log-rank test and Student *t*-test as appropriate. Statistical significance was set at $p<0.05$.

Results

Selective ablation of NMDA receptors in hippocampal CA3 pyramidal neurons

We disrupted the NMDA receptor *GluRζ1/NR1* gene specifically in the hippocampal CA3 pyramidal cells by Cre-*loxP* recombination on the C57BL/6N genetic background. By crossing a target mouse line carrying two *loxP* sequences flanking exon 19 and 20 of the *GluRζ1* gene (*GluRζ1*$^{+/flox}$ mice) with a hippocampal CA3 region-dominant Cre mouse line carrying the Cre recombinase gene inserted into the *GluRγ1/KA-1* gene (GluRγ1-Cre mice), we obtained *GluRγ1*$^{+/cre}$; *GluRζ1*$^{flox/flox}$ mice and *GluRζ1*$^{flox/flox}$ mice (Fig. 1), and used them in subsequent experiments as mutant and control mice, respectively.

In situ hybridization signals for the *GluRζ1* mRNA were indistinguishable between mutant and control mice at postnatal day 1 (P1) (Fig. 2A). At P7, *GluRζ1* signals were diminished specifically in the hippocampal CA3 region of mutant mice (Fig. 2B). At P21 to P23, the hybridization signals were hardly detectable in the CA3 region of mutant mice and slightly decreased in the brainstem (Fig. 2C). Residual hybridization signals for the *GluRζ1* mRNA were co-localized with those of the *GAD67* mRNA, suggesting that expression of the *GluRζ1* mRNA was intact in CA3 interneurons (Fig. 2G, $n = 17$ out of 17 GAD67-positive cells). Immunohistochemical analyses showed that immunoreactivity for GluRζ1 protein was present in the CA3 region at P7, though the amount appeared to be decreased (Fig. 2D). However, the expression of GluRζ1 protein was diminished to a negligible level at P14 and P21 (Fig. 2E and F).

We examined NMDA-EPSCs by whole-cell patch-clamp recordings from the pyramidal cell in the CA3 region of the hippocampus at P21 to P23. NMDA-EPSCs were evoked by stimulating associational/commissural fibers that mainly terminate in the stratum radiatum since NMDA receptors are more

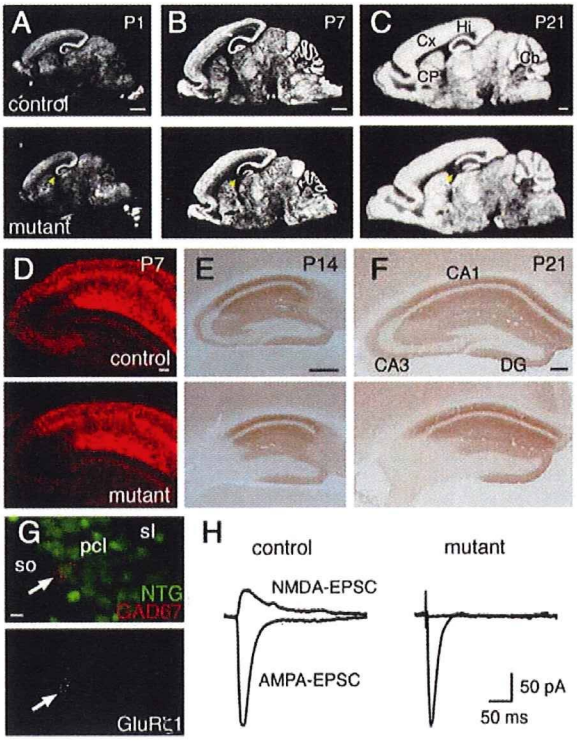

Figure 2. Generation of CA3 pyramidal neuron-selective NMDA receptor knockout mice. A–C, X-ray film autoradiography for *GluRζ1* mRNAs. Arrowheads indicate the CA3 region. **D–F**, Immunohistochemistry for GluRζ1 proteins. **G**, Double *in situ* hybridization for *GluRζ1* (white) and *GAD67* mRNA (red), counterstained with neurotrace green (green), in the mutant CA3 region. Arrow indicates a neuron expressing both *GluRζ1* and *GAD67* mRNAs. Scale bars: **A–C**, 1 mm; **D–F**, 200 µm; **G**, 10 µm. Abbreviations: Cb, cerebellum; CP, caudate-putamen; Cx, cortex; DG, dentate gyrus; Hi, hippocampus; pcl, pyramidal cell layer; sl, stratum lucidum; so, stratum oriens. **H**, Representative traces of AMPA- and NMDA-EPSCs at CA3 commissural/associational synapses.
doi:10.1371/journal.pone.0003993.g002

abundantly expressed in the stratum radiatum than in the stratum lucidum (Fig. 2H). In mutant mice, NMDA-EPSCs were not detectable, while AMPA-EPSCs were normally evoked. The ratios of the amplitudes of NMDA-EPSCs to those of AMPA-EPSCs were 50.9±16.1% (mean±s.e.m.) in control mice and 0.2±0.2% in mutant mice ($n = 4$ each; *t*-test, $P = 0.03$). Thus, NMDA receptors were abolished in hippocampal CA3 pyramidal neurons of mutant mice by P21. We used mutant and control mice at P21 to P23 in the following experiments unless otherwise specified.

Enhanced susceptibility of mutant mice to kainate-induced seizure

To monitor the excitability of CA3 recurrent circuits *in vivo*, we tested the kainate sensitivity of mutant mice since the administration of kainate to rodents stimulates initially the CA3 region and then generates seizures [37]. Intraperitoneal administration of kainate at 8 mg/kg induced tonic-clonic seizures with loss of the postural tone in mutant mice within 1 h, but not in control mice (Fig. 3A, $P<0.001$, Fisher's exact probability test). Mice of both genotypes showed seizures at a higher dosage of kainate (12 mg/kg), but the latency to the onset of seizures was significantly shorter in mutant mice (Fig. 3B, $P = 0.03$, log-rank test). Neither mutant

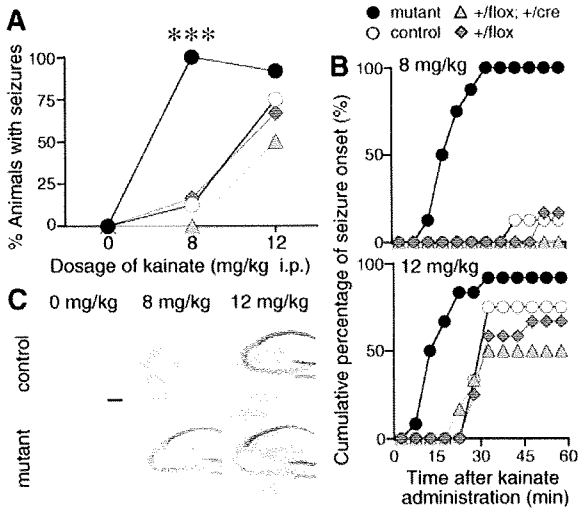

Figure 3. Increased susceptibility to kainate-induced tonic-clonic seizures in the mutant mice. A, The graph represents the percentage of mice with the generalized tonic-clonic seizures 1 h after drug administration. ***, $P<0.001$, Fisher's exact probability test. **B**, Cumulative curves for the onset of seizure. Saline, $n=4$–6; 8 mg/kg, $n=7$–8; 12 mg/kg, $n=12$. **C**, c-Fos immunohistochemistry in the hippocampus. Scale bar, 200 μm.
doi:10.1371/journal.pone.0003993.g003

nor control mice showed seizures after saline-administration. These results suggest that kainate-induced seizure susceptibility was enhanced in mutant mice. Susceptibility to the seizure was comparable between control *GluRζ1*$^{flox/flox}$ mice and *GluRγ1*$^{+/cre}$; *GluRζ1*$^{+/flox}$ mice, indicating that the insertion of the *Cre* gene in one allele of *GluRγ1* locus did not influence the susceptibility.

To monitor the neuronal activity *in vivo*, we employed c-Fos immunohistochemistry. There was little c-Fos immunoreactivity in the hippocampus of both control and mutant mice administrated with saline ($n=3$, Fig. 3C). Administration of kainate at 8 mg/kg induced strong c-Fos-immunoreactivity in the hippocampus of mutant mice ($n=3$). In contrast, no significant immunoreactivity was detectable in the hippocampus of kainate-administrated control mice ($n=3$). Kainate at 12 mg/kg induced strong c-Fos immunoreactivity in both control and mutant mice with seizures, while the number of Fos-immunopositive cells in the hippocampus was significantly smaller in mutant mice than in control mice ($n=20$ sections from 5 mice). The cellular imaging of neural activity with c-Fos immunohistochemistry confirmed the enhanced seizure susceptibility of mutant mice.

Histological features of the hippocampal CA3 region

Unexpectedly, we found that mutant mice lacking NMDA receptors selectively in CA3 pyramidal neurons became more susceptible to kainate-induced seizures. One obvious possibility is that the ablation of NMDA receptors may disturb the neural wiring of the hippocampal CA3 region, leading to abnormal excitability of the network. We thus examined the histological features of the hippocampal CA3 region in detail. The laminar organization and cellular distribution of the hippocampal CA3 region examined by Nissl staining was indistinguishable between control and mutant mice (Fig. 4A). Immunostaining for vesicular glutamate transporter 2 (VGluT2) and calbindin showed that the afferent terminals from the entorhinal cortex and the dentate gyrus were localized in the stratum lacunosum-moleculare and the stratum lucidum in both control and mutant mice, respectively (Fig. 4B and C).

Golgi staining revealed no appreciable differences in dendritic arborization of CA3 pyramidal cells between control and mutant mice (Fig. 4G). There were no significant differences in the numbers of branch points (control, 16.6±1.1, $n=8$; mutant, 17.0±1.1, $n=9$; $P=0.80$; *t*-test) and the primary (control, 4.4±0.5; mutant, 3.8±0.6; $P=0.45$), secondary (control, 7.8±0.7; mutant, 7.0±0.7; $P=0.49$) and tertiary dendrites (control, 9.4±1.4; mutant, 9.9±1.0; $P=0.76$) between two genotypes (Fig. 4I and J). Mean spine density on basal dendrites of CA3 pyramidal cells was also comparable ($n=28$ dendrites from 3–4 mice, $P=0.15$) (Fig. 4H and K). Consistent with Golgi staining, fine structures of CA3 neurons visualized by EGFP expression revealed no detectable alteration in terms of dendritic arborization and the distribution of presynaptic axonal boutons and postsynaptic spines (Fig. 5).

Immunoreactivities for postsynaptic proteins, PSD-95 and GluRα1/GluR1, were comparable in the hippocampal CA3 region between the two genotypes (Fig. 4D and E). Distribution of interneurons in the hippocampal CA3 and hilar areas was also indistinguishable as judged by immunostaining for GAD proteins (Fig. 4F), parvalbumin, somatostatin and calretinin. Thus, the histological and cytological organizations of the hippocampal CA3 region were indistinguishable between control and mutant mice.

Characteristic EEG spikes associated with multiple unit activities in the hippocampal CA3 region of mutant mice

Since seizure is produced by synchronous firing of a population of neurons in the brain [38], it is possible that NMDA receptor ablation in the CA3 region may modify hippocampal network oscillations *in vivo*. By recording local field potentials *in vivo* from the hippocampal CA3 region of urethane-anaesthetized mutant mice at the age of postnatal 8 weeks, we found characteristic spikes with large amplitudes (1.5–4.0 mV) (Fig. 6A). These EEG spikes were consistently observed in all 6 mutant mice, but never detected in 7 control mice. The mean firing rate of the spikes ($n=136$ from 6 mice) was 0.23±0.02 Hz and the distribution of interspike intervals showed a peak at 4.75 s (Fig. 6B).

To investigate the origin of characteristic EEG spikes, we recorded field potentials in various hippocampal regions of mutant mice using a silicon probe with 16 recording sites. Simultaneous recording of a single EEG spike event from the hippocampal CA3 region and surrounding neocortex showed that the amplitude of EEG spikes was largest in the CA3 pyramidal cell layer. EEG spikes reversed their polarity in the CA3 stratum oriens (Fig. 6C). Current source density (CSD) analysis of EEG spikes revealed a current sink in the CA3 pyramidal cell layer, with a source nearby ($n=8$ from 4 mice). Recording from the cortex and hippocampal CA1 region, spikes reversed their polarity in the CA1 stratum oriens. CSD analyses revealed a large sink in the CA1 pyramidal cell layer ($n=8$ from 4 mice). On the other hand, EEG spikes recorded from the dentate gyrus showed neither polarity reversal nor sinks in CSD maps ($n=8$ from 4 mice). These results suggest that characteristic spikes are generated in the pyramidal cell layers of the CA3 and CA1 regions, but not in the dentate gyrus.

Further analysis revealed that the frequency of MUA in the CA3 pyramidal cell layer was enormously high during spike events (Fig. 6D, center). The strong correlation between MUA and EEG spikes was observed in all 4 mutant mice. After EEG spikes, MUA in the CA3 pyramidal cell layer became silent (Fig. 6D, center). MUA in the CA1 pyramidal cell layer were also associated with EEG spikes (Fig. 6D, right) and the association was reproducibly observed in all 4 mutant mice. On the other hand, there was no

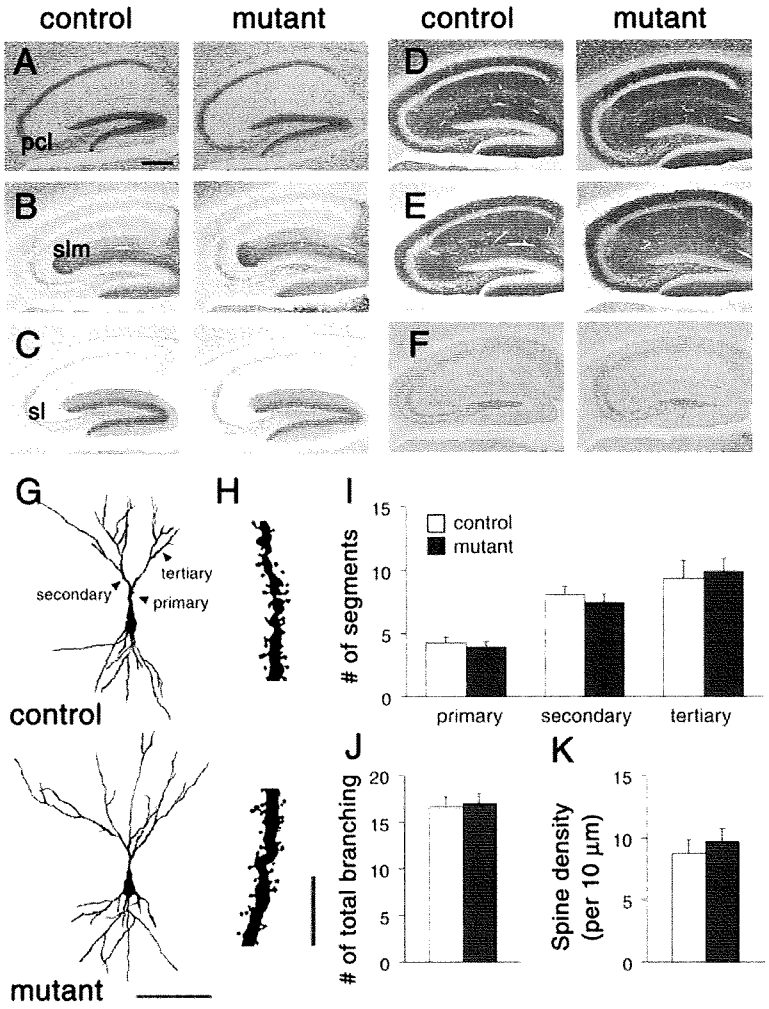

Figure 4. Normal histological organization of the hippocampal region. A, Nissl staining. **B, C**, Immunoperoxidase staining for VGluT2 (**B**) and Calbindin (**C**). **D–F**, Immunoperoxidase staining for PSD-95 (**D**), GluRα1 (**E**), and GAD (**F**). **G**, Cytoarchitecture of Golgi-stained CA3 pyramidal neurons. **H**, Higher magnification of the basal dendritic segment of CA3 pyramidal neuron in (**G**). **I–K**, Graphs represents the number of primary, secondary and tertiary dendrites (**I**), total number of dendritic branching (**J**), and spine density (**K**) of CA3 pyramidal neurons. Scale bars: **A**, 200 μm; **G**, 100 μm; **I**, 10 μm. Abbreviations: pcl, pyramidal cell layer; sl, stratum lucidum; slm, stratum lacunosum-moleculare.
doi:10.1371/journal.pone.0003993.g004

significant association in the dentate gyrus between MUA and spikes (Fig. 6D, left). The strong association of MUA with EEG spikes in the CA1 and CA3 pyramidal cell layers, but not in the dentate gyrus, together with CA3 pyramidal neuron-selective ablation of NMDA receptors, suggests that characteristic EEG spikes were originated from synchronous firing of CA3 pyramidal neurons and the activity of the CA3 network propagated to the downstream CA1 region.

Balanced excitatory and inhibitory synaptic transmission

Because either enhanced excitation or reduced inhibition can increase the excitability of hippocampal CA3 network, we examined the mRNA levels of excitatory glutamate receptor (GluR) subunits and glutamic acid decarboxylases (GADs) expressed in the hippocampal CA3 region of the mutant mice by *in situ* hybridization (Fig. 7A, Table 1). The *GluRζ1* mRNA was strongly diminished as described above. The reduction of the *GluRγ1* mRNA can be ascribed to the insertion of *cre* into one allele of the *GluRγ1* gene but the *cre* insertion exerted little effect on the kainate-induced seizure susceptibility as described above. There was no significant difference in the *GAD65* mRNA ($P=0.08$), while the level of *GAD67* mRNA was slightly but significantly reduced in the mutant mice ($P<0.001$). There were no significant differences in hybridization signals of other GluR mRNAs between control and mutant mice.

Basic electrophysiological properties of CA3 pyramidal cells were indistinguishable between two genotypes (resting membrane potential: control, -72.5 ± 0.8 mV, $n=32$; mutant -73.7 ± 1.0 mV, $n=26$, $P=0.37$; input resistance: control, 113.2 ± 5.3 MΩ; mutant, 117.7 ± 7.2 MΩ, $P=0.62$; membrane capacitance: control, 251.8 ± 9.4 pF; mutant, 250.2 ± 8.0 pF, $P=0.90$). We then compared $GABA_A$-IPSCs in the hippocampal CA3 region, which have been shown to suppress the excitability of the pyramidal cell through postsynaptic inhibition [39]. AMPA-EPSCs were evoked at −80 mV by stimulating afferent fibers in the CA3 stratum radiatum, which should activate both associa-

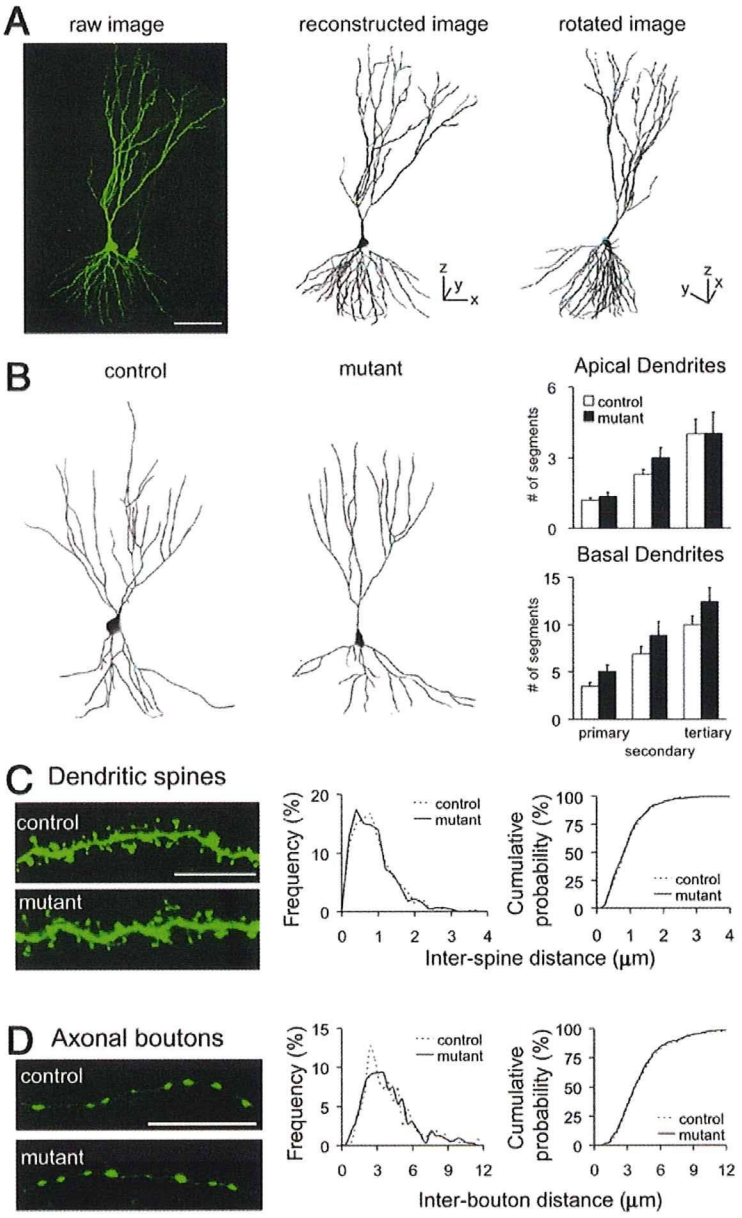

Figure 5. Dendritic branching and distribution of postsynaptic spines and presynaptic boutons in CA3 pyramidal neurons of control and mutant mice. **A**, Examples of three-dimensional reconstruction using IMARIS and FilamentTracer software. **B**, Three-dimensional reconstruction of AAV-EGFP-infected CA3 pyramidal neurons. Graphs represent the numbers of primary, secondary and tertiary dendrites of CA3 pyramidal neurons in control (open boxes, $n = 10–12$) and mutant mice (filled boxes, $n = 6–7$). There were no significant differences between control and mutant mice in the numbers of primary (apical, $P = 0.58$; basal, $P = 0.06$; *t*-test), secondary ($P = 0.13$, $P = 0.21$) and tertiary dendrites ($P = 1.0$ $P = 0.16$). **C**, Tertiary dendritic segments in control (left, top) and mutant (left, bottom) mice. Normalized distribution of inter-spine distances (middle, bin size, 0.1 μm). Cumulative distribution of inter-spine distances (right, same data set). There were no significant differences in inter-spine intervals of CA3 pyramidal neurons between two genotypes (control $n = 428$ from 10 dendrites of 4 mice; mutant, $n = 459$ from 9 dendrites of 4 mice; $P = 0.74$, Kolmogorov-Smirnov test). **D**, Boutons on the axon in the CA3 stratum radiatum of control (left, top) and mutant (left, bottom) mice. Normalized distribution of inter-bouton distances (middle, bin size, 0.4 μm). Cumulative distribution of inter-bouton distances (right, same data set). There were no significant differences in inter-bouton intervals of CA3 pyramidal neurons between two genotypes (control $n = 262$ from 18 axons of 4 mice; mutant, $n = 322$ from 24 dendrites of 4 mice; $P = 0.90$, Kolmogorov-Smirnov test).
doi:10.1371/journal.pone.0003993.g005

tional/commissural fibers and inhibitory interneurons (and their dendrites and axons), and then $GABA_A$-IPSCs were measured with the same stimulus strength at 0 mV in the presence of both the non-NMDA receptor antagonist CNQX and the NMDA receptor antagonist D-APV. The ratio of $GABA_A$-IPSCs to AMPA-EPSCs was indistinguishable between the two genotypes

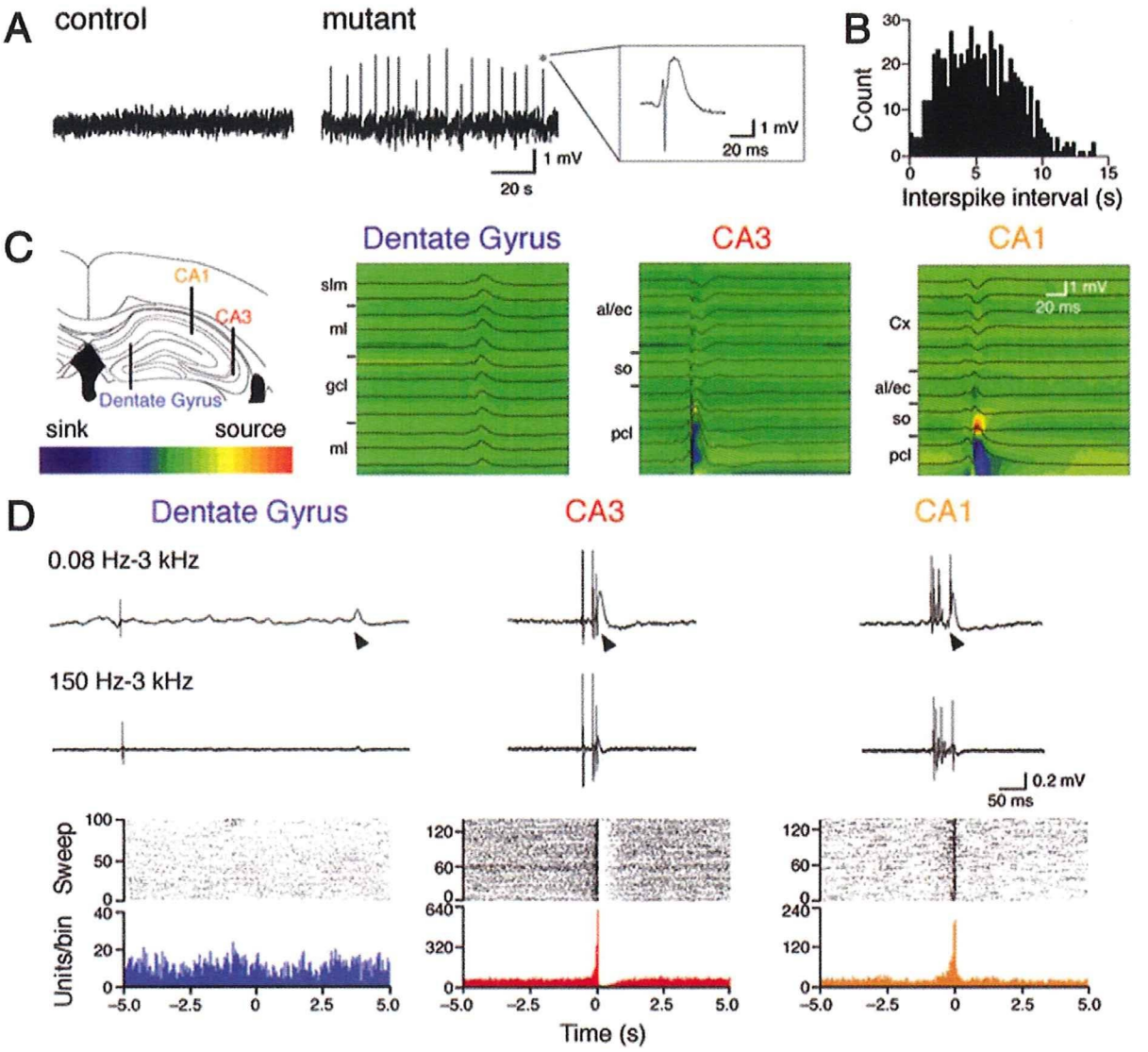

Figure 6. Characteristic large EEG spikes in the hippocampal CA3 region of mutant mice. A, Representative local field potential recordings from the CA3 region. **B**, Histogram of interspike intervals (bin, 0.25 s). **C**, Laminar profiles of field potentials and CSD analysis. Recording positions are illustrated on the left. Sinks and sources are indicated by cold and warm colors, respectively. Abbreviations: al/ec, alveus and external capsule; Cx, cortex; gcl, granule cell layer; ml, molecular layer; pcl, pyramidal cell layer; slm, stratum lacunosum-moleculare; so, stratum oriens. **D**, Wide-band recordings of extracellular activities (top), filtered MUA (middle) and raster plots and peri-event time histograms between MUA (bin, 200 ms) and EEG spikes in the dentate gyrus (left), CA3 (center) and CA1 regions (right). Arrowheads indicate the onset of spikes. MUA were aligned to the onset of spikes (time 0).

doi:10.1371/journal.pone.0003993.g006

(control, 0.52±0.09; mutant, 0.61±0.16; $n=12$ each; *t*-test, $P=0.65$) (Fig. 7B). Thus, there was no significant electrophysiological imbalance between AMPA receptor-mediated excitatory and $GABA_A$ receptor-mediated inhibitory synaptic transmission in the hippocampal CA3 region.

High-frequency stimulation failed to induce slow hyperpolarizing currents in hippocampal CA3 pyramidal neurons of mutant mice

In hippocampal CA1 pyramidal neurons, synaptic excitation is followed by an early GABA-mediated hyperpolarization and late AHP mediated by Ca^{2+}-dependent K^+ channels [40]. We thus examined the effect of NMDA receptor ablation on Ca^{2+}-dependent K^+ channels in hippocampal CA3 neurons. At a holding potential of −20 mV, high-frequency stimulation, which should activate both AMPA receptors and NMDA receptors in normal mice, induced slowly decaying outward currents in the pyramidal cells of control mice (Fig. 7C; peak amplitude, 46.1±5.4 pA, $n=12$). In contrast, such slow outward currents were hardly evoked by the same high-frequency stimulation in mutant mice (Fig. 7C; 0.5±2.1 pA, $n=12$, $P<0.001$). The outward currents in control mice were abolished by D-APV (Fig. 7D; control, 46.13±5.36 pA, $n=13$; D-APV, 0.38±2.41 pA, $n=12$,

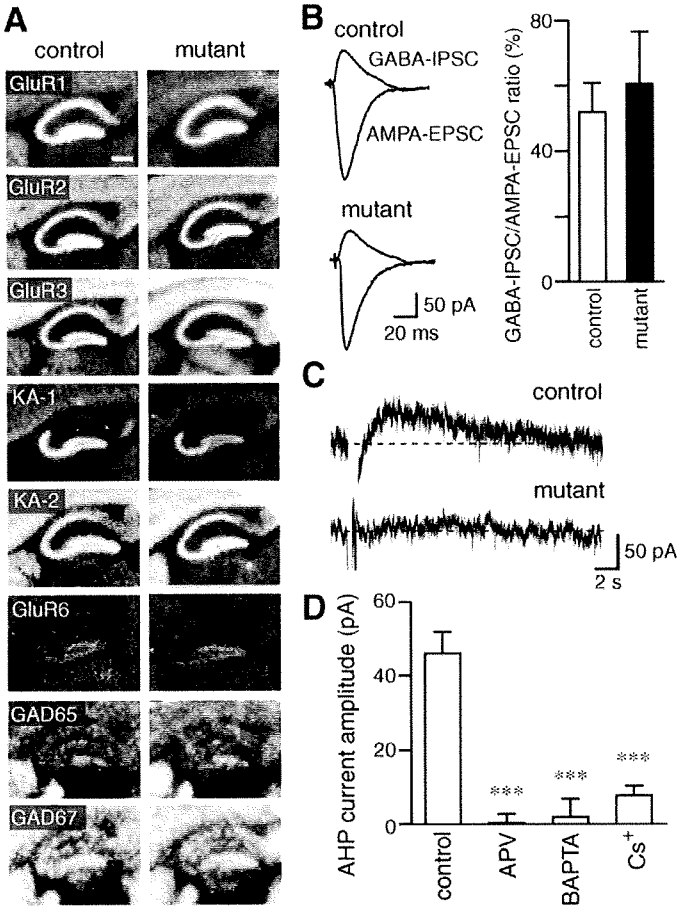

Figure 7. High-frequency stimulation failed to induce slow hyperpolarizing currents in hippocampal CA3 pyramidal neurons of mutant mice. A, X-ray film autoradiography for mRNAs of AMPA receptors, kainate receptors, and GADs. Scale bar, 200 μm. **B**, Representative traces of AMPA-EPSCs and $GABA_A$-IPSCs in the CA3 pyramidal cells. Graph shows the ratio of $GABA_A$-IPSCs to AMPA-EPSCs. **C**, Representative traces of slow hyperpolarizing currents. **D**, Peak amplitudes of the slow hyperpolarizing currents of the control mice in the absence (control) or presence of D-APV. Those recorded with a BAPTA-containing (BAPTA) or Cs^+-based internal solution (Cs^+) are also shown. ***, $P<0.001$, *t*-test.
doi:10.1371/journal.pone.0003993.g007

Table 1. Ratios of hybridization signal densities of GluR and GAD mRNAs in the CA3 region to those in the CA1 region.

mRNA	Control	Mutant
GluRζ1/NR1	0.86±0.02 ($n=10$)	0.04±0.01 ($n=5$)
GluRα1/GluR1	0.98±0.02 ($n=10$)	0.95±0.01 ($n=12$)
GluRα2/GluR2	0.91±0.03 ($n=8$)	0.89±0.03 ($n=11$)
GluRα3/GluR3	0.88±0.02 ($n=10$)	0.86±0.02 ($n=12$)
GluRγ2/KA-2	1.16±0.03 ($n=9$)	1.17±0.02 ($n=10$)
GluRβ2/GluR6	1.11±0.09 ($n=8$)	1.19±0.04 ($n=8$)
GAD65	1.12±0.05 ($n=10$)	0.99±0.05 ($n=11$)
GAD67	1.11±0.02 ($n=10$)	0.94±0.03 ($n=12$)

Slices were prepared from 3 mice of both genotypes.
Hybridization signal densities of the *GluRγ1/KA-1* mRNA in the CA3 region were 51.5±0.8 ($n=10$) in control mice and 32.3±0.5 ($n=12$) in mutant mice.
doi:10.1371/journal.pone.0003993.t001

$P<0.001$), suggesting that NMDA receptors are required for the response. NMDA receptor activation results in influx of Ca^{2+} into postsynaptic cells, which would activate Ca^{2+}-dependent K^+ channels. In fact, inclusion of the Ca^{2+} chelator BAPTA in the internal solution of patch pipettes diminished the outward currents (Fig. 7D; BAPTA, 1.99±4.76 pA, $n=7$, $P<0.001$). The outward currents were also diminished when recorded with a Cs^+-based internal solution (Fig. 7D; Cs^+, 7.74±2.35 pA, $n=4$, $P<0.001$), suggesting that the currents were mediated by postsynaptic K^+ channels. Taken together, the slow kinetics and sensitivities to D-APV, BAPTA and Cs^+ of the outward hyperpolarizing currents suggest that the high-frequency stimulation evokes slow AHP currents [41,42] mediated by Ca^{2+}-activated K^+ channels, which are activated by Ca^{2+} influx through NMDA receptor channels. These results suggest that the NMDA receptor-slow AHP coupling is diminished in the hippocampal CA3 pyramidal neurons of mutant mice, which may result in enhanced excitability of the CA3 recurrent network as a whole. The coupling between NMDA receptors and AHP currents is found in various regions [34,43–45]. However, the durations of AHP currents observed in our

experiment were much longer than those observed in previous studies.

These results with hippocampal CA3-specific NMDA receptor mutant mice raise an intriguing possibility that MDA receptors suppress the excitability of the CA3 recurrent network as a whole by restricting synchronous firing of CA3 neurons, although the possibility cannot be excluded that the enhanced excitability of the mutant mice might be due to subtle cytoarchitectural abnormalities of CA3 pyramidal neurons. To test the possibility, we then examined the effect of NMDA receptor ablation in the CA3 region of the adult brain on hippocampal network oscillations by employing a virus-mediated gene knockout technique [22,23].

Ablation of CA3 NMDA receptors in the mature brain also generated characteristic EEG spikes with large amplitudes

An adeno-associated viral expression vector for Cre recombinase (AAV-Cre, titer of $5–8\times10^{10}$) was streotaxically microinjected to the hippocampal CA3 region of *GluRζ1*$^{flox/flox}$ mice at 8–9 weeks old. Immunohistochemical analysis revealed that the infection of AAV-Cre was limited to the hippocampal CA3 region and spread within 40–70% of the region (Fig. 8A–C). Immunoreactivity for GluRζ1 was diminished in the well-demarcated infected CA3 region by 2 weeks after infection (Fig. 8C). Age-matched *GluRζ1*$^{+/+}$ mice microinjected with AAV-Cre served as controls.

Local field potential recording from the CA3 region showed characteristic EEG spikes with large amplitudes in *GluRζ1*$^{flox/flox}$ mice 2–3 weeks after AAV-Cre infection ($n=5$ out of 9 mice) (Fig. 8D). The frequency of large EEG spikes was variable among subjects, which may be related to the variance of AAV-infected regions among animals. No such spike activity was detected in EEG records from the CA3 region of AAV-Cre-infected *GluRζ1*$^{+/+}$ mice ($n=7$ out of 7 mice, $P=0.02$, Fisher's exact probability test) (Fig. 8D). CSD analysis revealed the sink in the pyramidal cell layer of the CA3 region and the sources in neighboring stratum oriens (Fig. 8E, $n=8$ spikes). Thus, the ablation of CA3 NMDA receptors induced by AAV-Cre infection in the adult brain also resulted in the generation of characteristic EEG spikes.

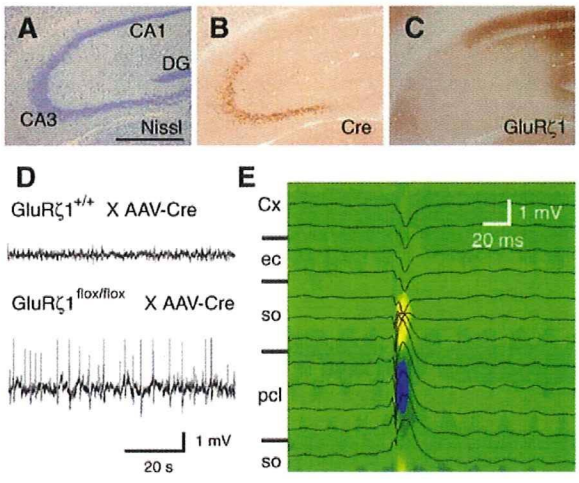

Figure 8. Hippocampal CA3 NMDA receptor ablation in the adult brain also generated characteristic EEG spikes with large amplitudes. A–C, AAV-Cre-mediated ablation of NMDA receptors in the hippocampal CA3 region. Nissl staining (**A**) and imunohistochemistry for Cre (**B**) and GluRζ1 (**C**). Scale bar, 0.5 mm. **D**, Representative local field potential recordings from the CA3 region. **E**, Laminar profiles of field potentials and CSD analysis. Recording positions are illustrated on the left. Sinks and sources are indicated by cold and warm colors, respectively. Cx, cortex; ec, external capsule; pcl, pyramidal cell layer; so, stratum oriens.
doi:10.1371/journal.pone.0003993.g008

Pharmacological blockade of CA3 NMDA receptors enhanced the susceptibility to kainate-induced seizure

We finally examined the seizure susceptibility of wild-type mice by focal injection of a competitive NMDA receptor antagonist, APV. We bilaterally injected 30 mM APV or aCSF into the hippocampal CA3 region of C57BL/6N mice at postnatal 8–10 weeks. About 20–30 minutes later, the animals were intraperitoneally administrated with the convulsive dose of kainate (30 mg/kg) [46]. Kainate-induced tonic-clonic seizures with loss of the postural tone appeared within 1 h in both groups of mice ($n=8$ each; $P=0.23$, Fisher's exact probability test) (Fig. 9). However, the latency to the onset of seizures was significantly shorter in mice injected with APV ($n=8$; $P=0.0044$, Log-rank test). Thus, the focal blockage of CA3 NMDA receptors also enhanced the susceptibility to kainate-induced seizure.

Discussion

Here, we generated hippocampal CA3 pyramidal neuron-specific NMDA receptor mutant mice on the C57BL/6N genetic background. The expression of the *GluRζ1* mRNA was comparable between mutant and control mice at P1 but strongly decreased in mutant mice at P7. The significant expression of GluRζ1 protein, though reduced, was found in the CA3 region at P7 but diminished to a negligible level by P14. We found that the mutant mice lacking NMDA receptors in the hippocampal CA3 pyramidal neurons showed enhanced susceptibility to kainate-induced seizures. This observation was rather unexpected since NMDA receptor-mediated LTP was implied to contribute to the generation of synchronous network activity by *in vitro* studies [14,15]. We found that characteristic EEG spikes with large amplitude were generated by the ablation of NMDA receptors in CA3 pyramidal neurons. Strong association of MUA with the characteristic EEG spikes in the CA3 pyramidal cell layer of mutant mice suggests that the CA3 NMDA receptor ablation increases the synchronous network activity possibly by affecting the firing pattern of CA3 neurons. In contrast, CA1 region-specific ablation of NMDA receptors appeared to hardly affect EEG *in vivo* [47]. NMDA receptor antagonists have minimal effects on basal synaptic transmission but completely block the generation of long-term potentiation in the CA1 region *in vitro* [48–50]. Hence, NMDA receptors in the CA1 region are not considered to be involved in spontaneous network activity. The difference in the neural wiring pattern such as the abundance of recurrent networks may underlie the different effects of NMDA receptor ablation in the hippocampal CA1 and CA3 regions on network activity. Our results raise an intriguing possibility that NMDA receptors may suppress the excitability of the CA3 network as a whole *in vivo*.

It is possible that the ablation of NMDA receptors may disturb the neural wiring of the hippocampal CA3 region, leading to abnormal excitability of the network. It is well known that the NMDA receptor plays a role in the activity-dependent refinement of synaptic connections and neural pattern formation [51–54]. Chronic blockade of NMDA receptors in hippocampal slice cultures during the first two weeks of postnatal development leads to a substantial increase in synapse number and results in a more complex dendritic arborization of CA1 pyramidal cells [31]. The activity blockade in hippocampus during postnatal 2–3 weeks by

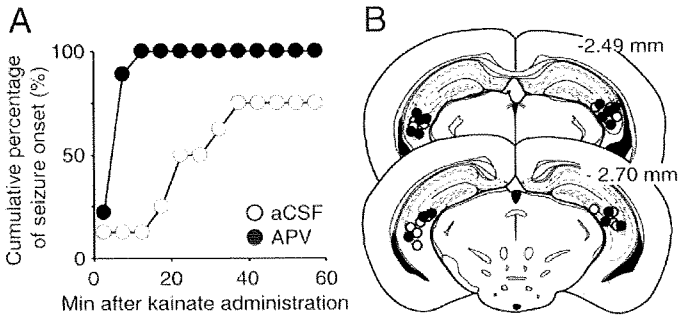

Figure 9. The pharmacological blockade of CA3 NMDA receptors increased the susceptibility to kainate-induced seizures. A, Cumulative curves for the onset of seizure. **B,** Illustration of the injection sites of APV (filled) and aCSF (open). Numbers represent distance (mm) of the section relative to the bregma landmark.
doi:10.1371/journal.pone.0003993.g009

tetrodotoxin infusion produced both behavioral and electrographic seizures 2 weeks after the infusion [55] and the increase in the density of axonal varicosities and postsynaptic AMPA receptor GluR1 and NMDA receptors [56]. Thus, reduced neuronal activity during development might potentially enhance the excitability. However, the cytoarchitecture was indistinguishable between control and mutant mice at P21–23. There were no detectable differences in the dendritic branching and the density of axonal boutons and dendritic spines between control and mutant mice at P21–23. The sustained expression of NMDA receptor proteins at least by P7 in mutant mice may support the development of CA3 pyramidal neuron cytoarchitectures. An alternative possibility is that the excitability of the CA3 network may be suppressed by NMDA receptor-mediated signaling. No significant differences were detectable in the basic membrane properties and balance between excitatory and inhibitory synaptic transmission between control and mutant mice. At synapses, activation of NMDA receptors evokes excitatory postsynaptic potential on the CA3 pyramidal neurons *in vitro* [57]. However, the enhancement of the kainate-induced seizure susceptibility and the emergence of characteristic EEG spikes associated with MUA in the mutant mice can be hardly explained if major roles of NMDA receptors would be simply mediating and strengthening the excitatory transmission at the commissural/associational synapses. Besides excitatory transmission and its enhancement, NMDA receptors may mediate diverse suppressive signals including spike-timing dependent long-term depression [58], LTP of slow GABA-IPSCs [59], the increase in I_h currents [60], and coupling with K^+ channels [34,43–45]. Thus, it is possible that NMDA receptor signaling may suppress the excitability of the CA3 network *in vivo*, although the possibility cannot be excluded that the enhanced excitability of the mutant mice might be due to subtle developmental abnormalities of CA3 pyramidal neurons.

We thus examined whether the excitability of the CA3 network is enhanced by ablation of NMDA receptors in the adult brain with a virus-mediated gene knockout technique [22,23]. We found that EEG spikes with large amplitude were generated by focal ablation of NMDA receptors in the CA3 region of adult mice by AAV-Cre infection. The frequency of large EEG spikes was variable among subjects, which may be related to the variance of AAV-infected regions among animals. Furthermore, the blockade of NMDA receptors by focal injection of APV into the hippocampal CA3 region enhanced the susceptibility to kainate-induced seizures. These results suggest that NMDA receptors control negatively the excitability of the hippocampal CA3 recurrent network as a whole *in vivo* by restricting synchronous firing of CA3 neurons, although the mechanism remains to be solved. Since slow AHP currents are involved in accommodation of action potential discharge of CA1 pyramidal neurons [40], it is possible that the frequency of action potentials may increase in a mutant CA3 pyramidal neuron where NMDA receptor-AHP coupling is eliminated. Prolonged discharges of CA3 pyramidal neurons might increase the chance of their synchronous firing, leading to the enhancement of the excitability of the CA3 network as a whole. Interestingly, Colgin et al. reported that blockade of NMDA receptors enhanced spontaneous sharp waves in rat hippocampal slices [61], supporting the idea that activation of NMDA receptors can serve to dampen the excitation of sharp waves. On the other hand, studies through computational models showed that when recurrent networks with conductance delays exhibit population bursts, spike-timing-dependent plasticity (STDP) rules exert a strong decoupling force that desynchronizes activity [58]. Thus, elimination of NMDA receptor-dependent STDP might enhance synchronization in CA3 recurrent networks. One or combination of such NMDA receptor-mediated suppressive signals [34,43–45,58–60] might underlie the regulation of CA3 network excitability. The NMDA receptors in the hippocampal CA3 region are implied in rapid acquisition and recall of associative memory as well as paired associate learning [11–13]. These functions may be mediated not only by the plasticity at synapses but also by the NMDA receptor-mediated neural network oscillation.

Acknowledgments

We thank Dr. H. Kashiwadani and Dr. K. Mori for valuable advice and help in field potential recordings and critical reading of the manuscript, Dr. Y. Kiyama for help in targeting vector construction, Ms R. Natsume for chimeric mouse preparation, Ms E. Kato for advice on Golgi staining, Mrs N. Takino and H. Nishida for technical assistance in AAV vector production, Ms A. Kishioka for help in animal surgery, Dr. T. Takeuchi for help in ES cell preparation, and Mrs H. Wakamatsu, Y. Takushi and T. Kurokawa for help in mice breeding. We are grateful to Dr. M. Ohtsuka for his encouragement and support. Thanks are also to Drs H. Iwama, I. Ito, Y. Takahashi and T. Tsujimoto for advice.

Author Contributions

Conceived and designed the experiments: FF KN MW TM MM. Performed the experiments: FF KN TS MF MW. Analyzed the data: FF KN TS MF MW. Contributed reagents/materials/analysis tools: SiM KS HK HM. Wrote the paper: FF KN MW TM MM.

References

1. Amaral DG, Witter MP (1989) The three-dimensional organization of the hippocampal formation: a review of anatomical data. Neuroscience 31: 571–591.
2. MacVicar BA, Dudek FE (1980) Local synaptic circuits in rat hippocampus: interactions between pyramidal cells. Brain Res 184: 220–223.
3. Miles R, Wong RK (1983) Single neurones can initiate synchronized population discharge in the hippocampus. Nature 306: 371–373.
4. Traub RD, Miles R (1991) Collective behaviours of the CA3 network: experiment and model. Neuronal Networks of The Hippocampus. Cambridge: Cambridge University Press. pp 119–156.
5. Buzsáki G (1989) Two-stage model of memory trace formation: a role for "noisy" brain states. Neuroscience 31: 551–570.
6. Jefferys JGR (1993) The pathophysiology of epilepsies. In: Laidlaw J, Richens A, Chadwick D, eds. A Textbook of epilepsy. 4th ed. Edinburgh: Churchill Livingstone. pp 241–276.
7. Csicsvari J, Hirase H, Czurko A, Buzsáki G (1998) Reliability and state dependence of pyramidal cell-interneuron synapses in the hippocampus: an ensemble approach in the behaving rat. Neuron 21: 179–189.
8. Ylinen A, Bragin A, Nádasdy Z, Jandó G, Szabó I, et al. (1995) Sharp wave-associated high-frequency oscillation (200 Hz) in the intact hippocampus: network and intracellular mechanisms. J Neurosci 15: 30–46.
9. Morris RG (2003) Long-term potentiation and memory. Philos Trans R Soc Lond B Biol Sci 358: 643–647.
10. Jonas P, Major G, Sakmann B (1993) Quantal components of unitary EPSCs at the mossy fibre synapse on CA3 pyramidal cells of rat hippocampus. J Physiol 472: 615–663.
11. Nakazawa K, Quirk MC, Chitwood RA, Watanabe M, Yeckel MF, et al. (2002) Requirement for hippocampal CA3 NMDA receptors in associative memory recall. Science 297: 211–218.
12. Nakazawa K, Sun LD, Quirk MC, Rondi-Reig L, Wilson MA, et al. (2003) Hippocampal CA3 NMDA receptors are crucial for memory acquisition of one-time experience. Neuron 38: 305–315.
13. Rajji T, Chapman D, Eichenbaum H, Greene R (2006) The role of CA3 hippocampal NMDA receptors in paired associate learning. J Neurosci 26: 908–915.
14. Bains JS, Longacher JM, Staley KJ (1999) Reciprocal interactions between CA3 network activity and strength of recurrent collateral synapses. Nat Neurosci 2: 720–726.
15. Behrens CJ, van den Boom LP, de Hoz L, Friedman A, Heinemann U (2005) Induction of sharp wave-ripple complexes in vitro and reorganization of hippocampal networks. Nat Neurosci 8: 1560–1567.
16. Yamazaki M, Mori H, Araki K, Mori KJ, Mishina M (1992) Cloning, expression and modulation of a mouse NMDA receptor subunit. FEBS Lett 300: 39–45.
17. Taniguchi M, Yuasa S, Fujisawa H, Naruse I, Saga S, et al. (1997) Disruption of semaphorin III/D gene causes severe abnormality in peripheral nerve projection. Neuron 19: 519–530.
18. Takeuchi T, Miyazaki T, Watanabe M, Mori H, Sakimura K, et al. (2005) Control of synaptic connection by glutamate receptor δ2 in the adult cerebellum. J Neurosci 25: 2146–2156.
19. Mishina M, Sakimura K (2007) Conditional gene targeting on the pure C57BL/6 genetic background. Neurosci Res 58: 105–112.
20. Takeuchi T, Nomura T, Tsujita M, Suzuki M, Fuse T, et al. (2002) Flp recombinase transgenic mice of C57BL/6 strain for conditional gene targeting. Biochem Biophys Res Commun 293: 953–957.
21. Werner P, Voigt M, Keinanen K, Wisden W, Seeburg PH (1991) Cloning of a putative high-affinity kainate receptor expressed predominantly in hippocampal CA3 cells. Nature 351: 742–744.
22. Li XG, Okada T, Kodera M, Nara Y, Takino N, et al. (2006) Viral-mediated temporally controlled dopamine production in a rat model of Parkinson disease. Mol Ther 13: 160–166.
23. Scammell TE, Arrigoni E, Thompson MA, Ronan PJ, Saper CB, et al. (2003) Focal deletion of the adenosine A1 receptor in adult mice using an adeno-associated viral vector. J Neurosci 23: 5762–5770.
24. Fukaya M, Kato A, Lovett C, Tonegawa S, Watanabe M (2003) Retention of NMDA receptor NR2 subunits in the lumen of endoplasmic reticulum in targeted NR1 knockout mice. Proc Natl Acad Sci U S A 100: 4855–4860.
25. Miyazaki T, Fukaya M, Shimizu H, Watanabe M (2003) Subtype switching of vesicular glutamate transporters at parallel fibre-Purkinje cell synapses in developing mouse cerebellum. Eur J Neurosci 17: 2563–2572.
26. Nakagawa S, Watanabe M, Isobe T, Kondo H, Inoue Y (1998) Cytological compartmentalization in the staggerer cerebellum, as revealed by calbindin immunohistochemistry for Purkinje cells. J Comp Neurol 395: 112–120.
27. Fukaya M, Watanabe M (2000) Improved immunohistochemical detection of postsynaptically located PSD-95/SAP90 protein family by protease section pretreatment: a study in the adult mouse brain. J Comp Neurol 426: 572–586.
28. Shimuta M, Yoshikawa M, Fukaya M, Watanabe M, Takeshima H, et al. (2001) Postsynaptic modulation of AMPA receptor-mediated synaptic responses and LTP by the type 3 ryanodine receptor. Mol Cell Neurosci 17: 921–930.
29. Yamada K, Fukaya M, Shimizu H, Sakimura K, Watanabe M (2001) NMDA receptor subunits GluRε1, GluRε3 and GluRζ1 are enriched at the mossy fibre-granule cell synapse in the adult mouse cerebellum. Eur J Neurosci 13: 2025–2036.
30. Watanabe M, Fukaya M, Sakimura K, Manabe T, Mishina M, et al. (1998) Selective scarcity of NMDA receptor channel subunits in the stratum lucidum (mossy fibre-recipient layer) of the mouse hippocampal CA3 subfield. Eur J Neurosci 10: 478–487.
31. Luthi A, Schwyzer L, Mateos JM, Gahwiler BH, McKinney RA (2001) NMDA receptor activation limits the number of synaptic connections during hippocampal development. Nat Neurosci 4: 1102–1107.
32. Fukaya M, Yamazaki M, Sakimura K, Watanabe M (2005) Spatial diversity in gene expression for VDCCγ subunit family in developing and adult mouse brains. Neurosci Res 53: 376–383.
33. Yamada K, Fukaya M, Shibata T, Kurihara H, Tanaka K, et al. (2000) Dynamic transformation of Bergmann glial fibers proceeds in correlation with dendritic outgrowth and synapse formation of cerebellar Purkinje cells. J Comp Neurol 418: 106–120.
34. Isaacson JS, Murphy GJ (2001) Glutamate-mediated extrasynaptic inhibition: direct coupling of NMDA receptors to Ca^{2+}-activated K^+ channels. Neuron 31: 1027–1034.
35. Murakami M, Kashiwadani H, Kirino Y, Mori K (2005) State-dependent sensory gating in olfactory cortex. Neuron 46: 285–296.
36. Franklin KBJ, Paxinos G (1996) The mouse brain in stereotaxic coordinates. San Diego: Academic Press.
37. Ben-Ari Y (1985) Limbic seizure and brain damage produced by kainic acid: mechanisms and relevance to human temporal lobe epilepsy. Neuroscience 14: 375–403.
38. Westbrook GL (2000) Seizures and Epilepsy. In: Kandel ER, Schwartz JH, Jessell TM, eds. Principles of Neural Science. 4th ed. Cambridge: Cambridge Univ Press. pp 910–935.
39. Lawrence JJ, McBain CJ (2003) Interneuron diversity series: containing the detonation—feedforward inhibition in the CA3 hippocampus. Trends Neurosci 26: 631–640.
40. Nicoll RA, Alger BE (1981) Synaptic excitation may activate a calcium-dependent potassium conductance in hippocampal pyramidal cells. Science 212: 957–959.
41. Schwartzkroin PA, Stafstrom CE (1980) Effects of EGTA on the calcium-activated afterhyperpolarization in hippocampal CA3 pyramidal cells. Science 210: 1125–1126.
42. Stocker M, Krause M, Pedarzani P (1999) An apamin-sensitive Ca^{2+}-activated K^+ current in hippocampal pyramidal neurons. Proc Natl Acad Sci U S A 96: 4662–4667.
43. Faber ES, Delaney AJ, Sah P (2005) SK channels regulate excitatory synaptic transmission and plasticity in the lateral amygdala. Nat Neurosci 8: 635–641.
44. Lin MT, Lujan R, Watanabe M, Adelman JP, Maylie J (2008) SK2 channel plasticity contributes to LTP at Schaffer collateral-CA1 synapses. Nat Neurosci 11: 170–177.
45. Ngo-Anh TJ, Bloodgood BL, Lin M, Sabatini BL, Maylie J, et al. (2005) SK channels and NMDA receptors form a Ca^{2+}-mediated feedback loop in dendritic spines. Nat Neurosci 8: 642–649.
46. Mulle C, Sailer A, Pérez-Otaño I, Dickinson-Anson H, Castillo PE, et al. (1998) Altered synaptic physiology and reduced susceptibility to kainate-induced seizures in GluR6-deficient mice. Nature 392: 601–605.
47. McHugh TJ, Blum KI, Tsien JZ, Tonegawa S, Wilson MA (1996) Impaired hippocampal representation of space in CA1-specific NMDAR1 knockout mice. Cell 87: 1339–1349.
48. Bear MF, Malenka RC (1994) Synaptic plasticity: LTP and LTD. Curr Opin Neurobiol 4: 389–399.
49. Bliss TV, Collingridge GL (1993) A synaptic model of memory: long-term potentiation in the hippocampus. Nature 361: 31–39.
50. Malenka RC, Nicoll RA (1999) Long-term potentiation—a decade of progress? Science 285: 1870–1874.
51. Cline HT, Debski EA, Constantine-Paton M (1987) *N*-methyl-D-aspartate receptor antagonist desegregates eye-specific stripes. Proc Natl Acad Sci U S A 84: 4342–4345.
52. Kleinschmidt A, Bear MF, Singer W (1987) Blockade of "NMDA" receptors disrupts experience-dependent plasticity of kitten striate cortex. Science 238: 355–358.
53. Kutsuwada T, Sakimura K, Manabe T, Takayama C, Katakura N, et al. (1996) Impairment of suckling response, trigeminal neuronal pattern formation, and hippocampal LTD in NMDA receptor ε2 subunit mutant mice. Neuron 16: 333–344.
54. Li Y, Erzurumlu RS, Chen C, Jhaveri S, Tonegawa S (1994) Whisker-related neuronal patterns fail to develop in the trigeminal brainstem nuclei of NMDAR1 knockout mice. Cell 76: 427–437.
55. Galvan CD, Hrachovy RA, Smith KL, Swann JW (2000) Blockade of neuronal activity during hippocampal development produces a chronic focal epilepsy in the rat. J Neurosci 20: 2904–2916.
56. Galvan CD, Wenzel JH, Dineley KT, Lam TT, Schwartzkroin PA, et al. (2003) Postsynaptic contributions to hippocampal network hyperexcitability induced by chronic activity blockade in vivo. Eur J Neurosci 18: 1861–1872.

57. Debanne D, Gähwiler BH, Thompson SM (1998) Long-term synaptic plasticity between pairs of individual CA3 pyramidal cells in rat hippocampal slice cultures. J Physiol 507: 237–247.
58. Lubenov EV, Siapas AG (2008) Decoupling through synchrony in neuronal circuits with propagation delays. Neuron 58: 118–131.
59. Huang CS, Shi SH, Ule J, Ruggiu M, Barker LA, et al. (2005) Common molecular pathways mediate long-term potentiation of synaptic excitation and slow synaptic inhibition. Cell 123: 105–118.
60. Fan Y, Fricker D, Brager DH, Chen X, Lu HC, et al. (2005) Activity-dependent decrease of excitability in rat hippocampal neurons through increases in I(h). Nat Neurosci 8: 1542–1551.
61. Colgin LL, Jia Y, Sabatier J-M, Lynch G (2005) Blockade of NMDA receptors enhances spontaneous sharp waves in rat hippocampal slices. Neurosci Lett 385: 46–51.

Cardiovascular Research (2009) 83, 682–687
doi:10.1093/cvr/cvp171

The cardiac pacemaker-specific channel *Hcn4* is a direct transcriptional target of MEF2

Shinobu Kuratomi[1], Yoko Ohmori[1], Masayuki Ito[1], Kuniko Shimazaki[1], Shin-ichi Muramatsu[2], Hiroaki Mizukami[3], Hideki Uosaki[4], Jun K. Yamashita[4], Yuji Arai[5], Koichiro Kuwahara[6], and Makoto Takano[1]*

[1]*Department of Physiology, School of Medicine, Jichi Medical University, Shimotsuke, Tochigi 329-0498, Japan;* [2]*Division of Neurology, Department of Medicine, School of Medicine, Jichi Medical University, Shimotsuke, Tochigi 329-0498, Japan;* [3]*Division of Genetic Therapeutics, Center for Molecular Medicine, Jichi Medical University, Shimotsuke, Tochigi 329-0498, Japan;* [4]*Laboratory of Stem Cell Differentiation, Stem Cell Research Center, Institute for Frontier Medical Sciences, Kyoto University, Kyoto 606-8507, Japan;* [5]*Department of Bioscience, National Cardiovascular Center Research Institute, Suita, Osaka 565-8565, Japan; and* [6]*Department of Medicine and Clinical Sciences, Graduate School of Medicine, Kyoto University, Kyoto 606-8507, Japan*

Received 21 January 2009; revised 8 May 2009; accepted 22 May 2009; online publish-ahead-of-print 28 May 2009

Time for primary review: 34 days

KEYWORDS
Hcn4;
MEF2;
Sino-atrial node;
Channel;
Transcription

Aims *Hcn4*, which encodes the hyperpolarization-activated, cyclic nucleotide-sensitive channel (I_h), is a well-established marker of the cardiac sino-atrial node. We aimed to identify *cis*-elements in the genomic locus of the *Hcn4* gene that regulate the transcription of *Hcn4*.

Methods and results We screened evolutionarily conserved non-coding sequences (CNSs) that are often involved in the regulation of gene expression. The VISTA Enhancer Browser identified 16 regions, termed CNS 1-16, within the *Hcn4* locus. Using the luciferase reporter assay in primary neonatal rat cardiomyocytes, we found that CNS13 conferred a prominent enhancer activity (more than 30-fold) on the *Hcn4* promoter. Subsequent mutation analysis revealed that the *Hcn4* enhancer function was dependent on myocyte enhancer factor-2 (MEF2) and activator protein-1 (AP1) binding sequences located in CNS13. Electrophoretic mobility shift assay and chromatin immunoprecipitation confirmed that MEF2 and AP1 proteins bound CNS13. Furthermore, overexpression of a dominant negative MEF2 mutant inhibited the enhancer activity of CNS13, decreased *Hcn4* mRNA expression and also decreased the amplitude of I_h current in myocytes isolated from the inflow tract of embryonic heart.

Conclusion These results suggest that the novel enhancer CNS13 and MEF2 may play a critical role in the transcription of *Hcn4* in the heart.

1. Introduction

The appropriate timing of cardiac muscle contraction is regulated by the electrical conduction system of the heart and consists of cardiomyocytes possessing specialized electrical function. The precise expression pattern of cardiac ion channel genes in relation to such electrophysiological properties has been extensively studied.[1,2] Previous reports have demonstrated that the hyperpolarization-activated, cyclic nucleotide-sensitive cation current (I_h) encoded by the *Hcn4* gene appears one of the ion currents underlying pacemaker depolarization.[3,4] In mammalian adult heart, *Hcn4* is specifically expressed in the sino-atrial node (SAN). During development *Hcn4* is also expressed in the foetal and neonatal chamber myocardium. As a result of this distribution, *Hcn4* is now recognized as a key marker gene of the SAN.[5,6] Despite its role as an SAN marker, little is known about the *cis*-elements that directly regulate *Hcn4* expression. Progress in the genome project and comparative genomic-base approaches have proven useful in the identification of gene regulatory sequences in a wide range of genomic loci.[7,8] We have previously reported that an 847 bp proximal sequence induces minimal promoter activity of the *Hcn4* gene.[9] In addition to this proximal upstream region, we also identified conserved, non-coding sequences within the *Hcn4* gene locus and analysed their enhancer function. We found that the novel enhancer contained binding sites for activator protein-1 (AP1) and myocyte enhancer factor-2 (MEF2) and played a critical role in the expression of *Hcn4*. These results outline the potential mechanisms underlying SAN differentiation.

* Corresponding author. Tel: +81 285 58 7308; Fax: +81 285 40 6294.
E-mail address: takanom@jichi.ac.jp

2. Methods

2.1 Construction of the promoter reporter plasmid

Luciferase reporter constructs were prepared using pGL4.10 vector (Promega) and the *Hcn4* promoter construct was obtained as previously described.[9] Conserved non-coding sequence (CNS) fragments were isolated from mouse genomic DNA by PCR with the primer pairs listed in Supplementary material online, *Table S1* and were subcloned into the upstream region of the *Hcn4* promoter.

2.2 Cell culture

For the culture of neonatal cardiomyocytes, 1- to 2-day-old rats were decapitated, the ventricle rapidly dissected and myocytes isolated by collagenase digestion (Worthington, type 2, 80 U/mL). The myocytes were then enriched by discontinuous Percoll gradient centrifugation (yield more than 90%).

For the culture of embryonic cardiomyocytes, rat embryos (13 days after fertilization) were removed from pregnant rats under deep anaesthesia with ether, the inflow tract of embryonic heart dissected and the primordial right and left appendixes removed. Myocytes were then isolated using the same procedure as that for the culture of neonatal myocytes.

Embryonic and neonatal cardiomyocytes were plated at a density of 2×10^4 and 10^5 cells/well, respectively, in 24-well plates and cultured in DMEM with 10% foetal bovine serum.[9]

All experiments were approved in advance by the animal Ethics Committee of Jichi Medical University. The investigation conforms with the Guide for the Care and Use of Laboratory Animals published by the US National Institutes of Health (NIH Publication No. 85-23, revised 1996).

2.3 Luciferase reporter gene assay

Luciferase reporter constructs (0.5 μg) and pGL4.74 vector (0.03 μg) were co-transfected into neonatal cardiomyocytes using Lipofectamine LTX (Invitrogen). Luciferase activities were measured 3 days after the transfection using the Dual-Luciferase Reporter Assay System (Promega). Transcriptional activities were obtained from three separate assays performed in quadruplicate.

2.4 Electrophoretic mobility shift assays

The myc-tagged mouse c-Jun/AP1 and MEF2C proteins were *in vitro* translated using TNT Quick Coupled Transcription/Translation System (Promega) and CNS13 DNA probes radiolabelled with [^{32}P]. The binding reaction was then performed in a reaction buffer (final volume=20 μL) containing 20 mM HEPES (pH 7.6), 50 mM KCl, 1 mM $MgCl_2$, 0.1% Nonidet P-40, 5% glycerol, 5 mM dithiothreitol, 1 mM EDTA, and 1 μg poly(dI-dC). The probe (10 fmol) incubated with 1 μL of protein was analysed on 4% polyacrylamide gels in ×0.25 TBE buffer. In competition experiments, 100-fold molar excess of double-strand oligonucleotides (AP1: 5′-ATT CTG AGT CAG AGA-3′ and MEF2: 5′-AGG TGG GTT AAA AAT AGA GCC CT-3′) were added.

2.5 Chromatin immunoprecipitation

Chromatin isolated from neonatal rat cardiomyocytes was immunoprecipitated with specific antibodies directed against anti-c-Jun/AP1 (Calbiochem) and anti-MEF2 (AnaSpec) using the EZ chromatin immunoprecipitation (ChIP) assay kit (Upstate) and analysed by PCR using the following primer pairs: CNS13 ChIP primers 5′-CCT TGG TTG TGA GTC TGT GTC T-3′ (forward) and 5′-AGT GGA GAG ACT GCT CTT TTC C-3′ (reverse) and control ChIP primers 5′-AAT GGG ACT CCT CTT ACT CAT TTC T-3′ (forward) and 5′-AAA GTC CCT GAT GAC ACA CTA GTT C-3′ (reverse).

2.6 AAV vector production and transfection

Adeno-associated virus (AAV) vector plasmids contain an expression cassette consisting of a CMV promoter followed by the first intron of human growth hormone, target cDNA, woodchuck hepatitis virus post-transcriptional regulatory element (GenBank accession no. J04514) and the SV40 poly-A signal sequence, between the inverted terminal repeats of the AAV-3 genome. The plasmids pAAV-dnMEF2 and pAAV-GFP contained the cDNA of the dominant negative MEF2 (dnMEF2) fused with Orange fluorescent protein (Clontech) and GFP, respectively. The two helper plasmids, pHelper (Agilent) and pAAV1-RC, harbour the *E2A*, *E4*, and *VA RNA* genes of the adenovirus genome, and the AAV-1 *rep* and *cap* genes, respectively. HEK293 cells were cotransfected using the calcium phosphate coprecipitation method with the vector plasmid, pAAV1-RC and pHelper. AAV1 vectors were harvested and purified via two sequential continuous iodoxale ultracentrifugations. The vector titer was determined by quantitative PCR (Q-PCR) of DNase I-treated vector stocks, yielding 10^{11}–10^{12} vector genome copies (vg).[12] 2×10^4 foetal myocytes were transfected with 10^{10} vg AAV1-dnMEF2 or AAV1-EGFP; and 10^5 vg Empty AV5 vector was also transfected as a helper.

2.7 RT-PCR and Q-PCR analysis

Three days after the transfection of AAV1, total RNA was isolated from primary cultured embryonic myocytes using TRIZOL reagent (Invitrogen). Single-strand cDNA was synthesized using Superscript III (Invitrogen). Q-PCR was carried out with predesigned Taqman Probes for *hcn4*, *hcn2*, *hcn1*, *stars*, and the 18s rRNA, in an ABI Prism 7700 System (Applied Biosystems).

2.8 Immunostaining of cardiomyocytes

Cardiomyocytes were fixed with 4% paraformaldehyde and incubated with primary antibodies directed against HCN4 (1:200 dilution; Chemicon) and actinin (1:750; Monoclonal, Sigma). Following extensive washes, cells were incubated with Alexa Fluor 488-conjugated anti-rabbit or anti-mouse Ig secondary antibodies at a concentration of 1:500 (Molecular Probes).

2.9 Electrophysiological analysis

Electrophysiological measurements were carried out using an Axopatch200B amplifier and a Digidata 1320 interface (Axon). The bathing solution contained 140 mM NaCl, 5.4 mM KCl, 0.33 mM NaH_2PO_4, 0.5 mM $MgCl_2$, 1.8 mM $CaCl_2$, 0.5 mM $BaCl_2$, 5 mM HEPES (pH 7.4 with NaOH), and the standard high K^+ pipette solution contained 110 Aspartic acid, 30 mM KCl, 5 mM MgATP, 5 mM Na_2 creatine phosphate, 0.1 mM Na_2GTP, 2 mM EGTA, 10 mM HEPES (pH 7.2 with KOH).

2.10 Statistical analysis

Data are expressed as mean ± SD values. Statistical analysis was performed using the Student's *t*-test and $P < 0.05$ was defined as statistically significant.

3. Results

3.1 Functional analysis of conserved non-coding regions within the *Hcn4* gene locus

Our previous study revealed that the proximal 847 bp sequence in the *Hcn4* upstream region is essential for promoter activity.[9] In order to locate additional *cis*-regulatory sequences, we extensively searched the CNSs in the genomic locus of *Hcn4*. As illustrated in *Figure 1A*, we identified 16 regions using VISTA Enhancer Browser, and designated these regions CNS 1-16 (Supplementary material online, *Table S1*).[8]

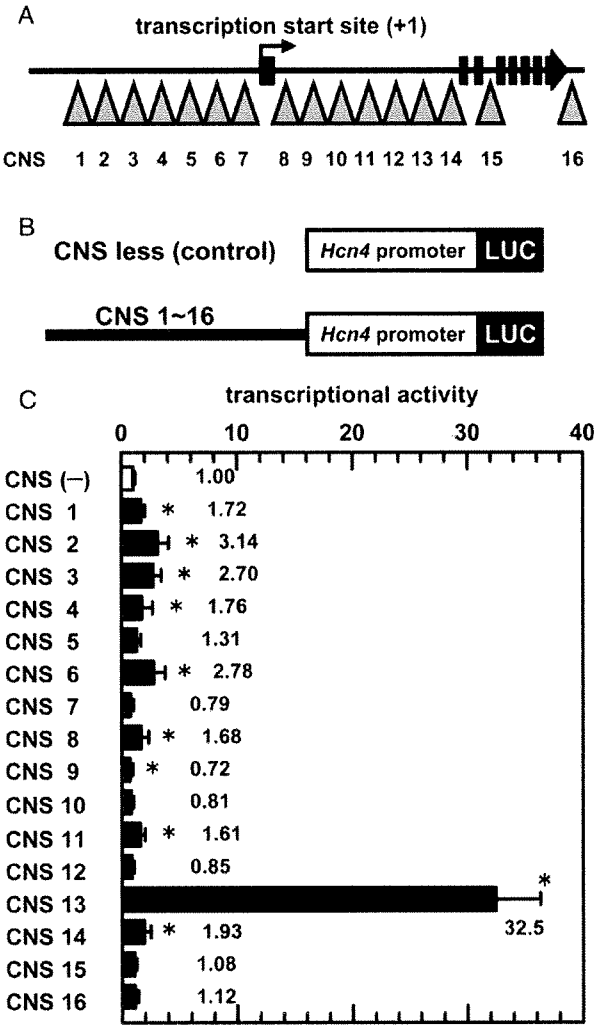

Figure 1 Enhancer activity of the CNS fragments. (*A*) A schematic diagram outlining the genomic organization of the murine *Hcn4* gene. Arrows indicate CNS regions. (*B*) Structure of the luciferase reporter constructs. The *Hcn4* promoter comprises nucleotides −446 to +400 relative to the transcription start site. (*C*) Enhancer activity conferred by the CNS fragments. Data are presented as relative values to the activity of the *Hcn4* promoter. $^*P < 0.05$ compared with construct of *Hcn4* promoter alone.

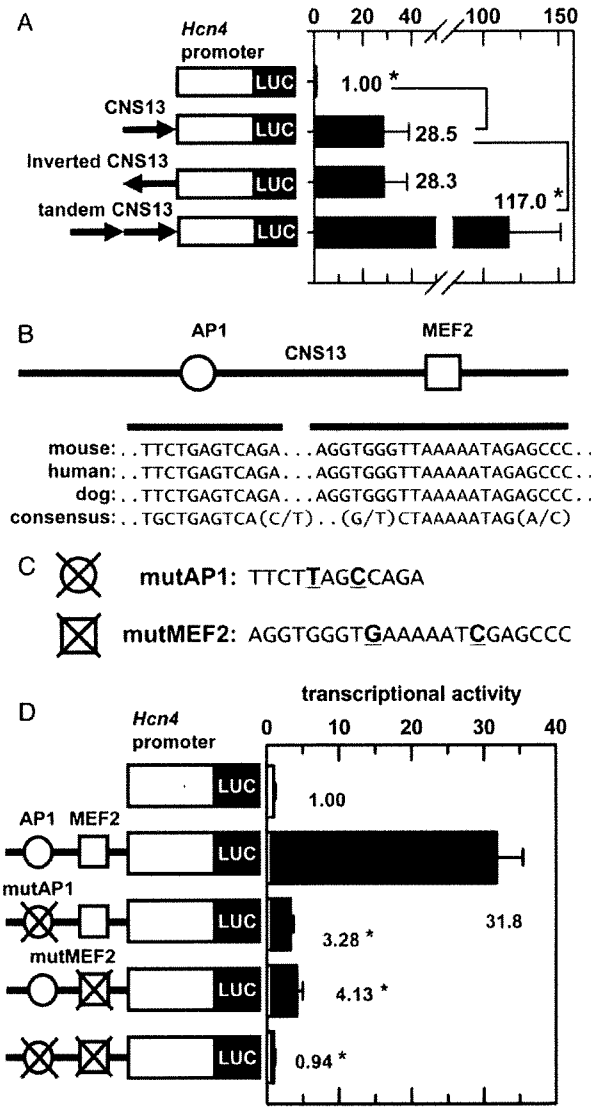

Figure 2 MEF2 and AP1 sites are essential in CNS13. (*A*) A schematic diagram of control, inverted, and tandem CNS13 constructs. The inverted construct was made by swapping the restriction sites at the ends of the control CNS13 fragment. The tandem construct, by introducing *Eco*RI site between the fragments. $^*P < 0.05$ compared with control CNS13 construct. (*B*) A schematic diagram of the putative binding sequences for AP1 (open circle) and MEF2 (open square) in CNS13. The AP1 and MEF2 sequences in mouse, human, and dog are aligned with the consensus sequences. The score for the matches were AP1: core match 1.000; matrix match 0.923. MEF2: core match 1.000; matrix match 0.957. (*C*) Mutation of the AP1 and MEF2 sites. The bold, underlined characters indicate the substituted nucleotides. (*D*) Enhancer activity of the CNS13 mutants. Data is presented as relative values to the activity of the *Hcn4* promoter. $^*P < 0.05$ compared with *Hcn4* promoter.

We next evaluated enhancer activity for each of the CNS regions using the luciferase reporter assay. In order to achieve this, we linked CNS fragments to the *Hcn4* promoter expressing the luciferase reporter gene in the pGL4.10 vector (*Figure 1B*) and analysed enhancer function in cultured primary cardiomyocytes. As shown in *Figure 1C*, nine CNS fragments (CNS1, 2, 3, 4, 6, 8, 11, 13, and 14) significantly enhanced *Hcn4* promoter activity. The CNS13 construct led to an ~33-fold increase in transcriptional activity, in comparison to the remainder of the constructs that resulted in no more than a 3.2-fold increase.

3.2 MEF2 and AP1 sites are required for the enhancer activity of CNS13

To confirm that CNS13 acts as an authentic enhancer, we next constructed inverted CNS13 and tandem repeated CNS13 fragments and fused with the *Hcn4* promoter. As shown in *Figure 2A*, no significant difference was found between the enhancer activities of normal- and inverted-CNS13 fragments. Tandem repeat CNS13 robustly activated the *Hcn4* promoter. We then focused our study on the CNS13 sequence and explored its *cis*-regulatory mechanism and its potential as a novel enhancer for the *Hcn4* promoter.

To characterize functional motifs in the CNS13 sequence, we searched putative transcription factor binding sites using

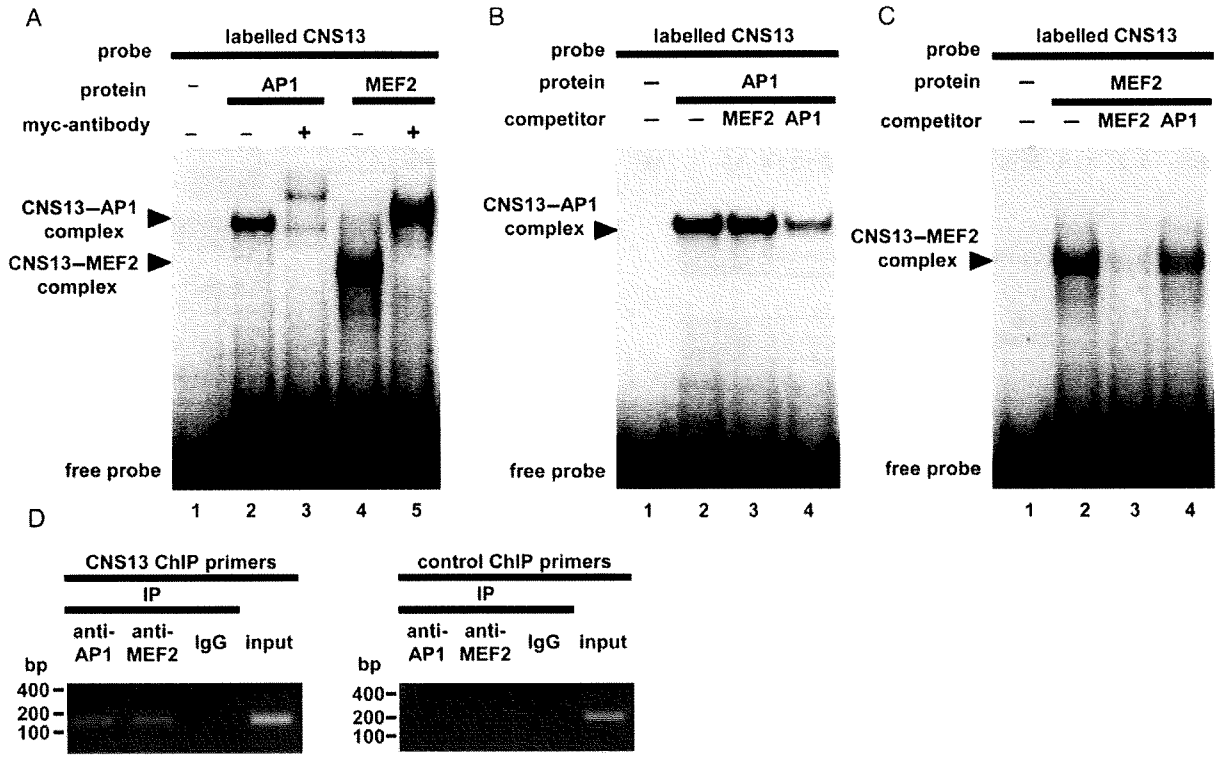

Figure 3 Electrophoretic mobility shift assay (EMSA) and chromatin immunoprecipitation (ChIP) assay using a radiolabelled CNS13 probe. (*A*) EMSA with myc-tagged AP1 and MEF2 proteins. The myc-antibody was used for the supershift assay. (*B*) Competitive EMSAs for the CNS13–AP1 complex. (*C*) CNS13–MEF2 complexes. (*D*) ChIP products using specific antibodies directed against AP1 and MEF2, or a pre-immune IgG were analysed by PCR. Input lane represents PCR products amplified from sonicated chromatin prior to immunoprecipitation. The 152 bp (left) and 200 bp (right) products correspond to CNS13 and distinct genomic regions, respectively.

the TRANSFAC database and detected MEF2- and AP1-binding motifs. As shown in *Figure 2B*, the putative MEF2- and AP1-binding sequences are perfectly conserved among several mammalian species and closely resemble their consensus sequences. These motifs, however, were not conserved in non-mammalian species. We prepared CNS13 reporter constructs harbouring mutations within the MEF2 and AP1 sites (*Figure 2C*) and examined whether enhancer activity was mediated by these sites. As shown in *Figure 2D*, a single mutation in either MEF2- or AP1-binding sequences significantly reduced transcriptional activity, whereas double mutations completely abolished CNS13-induced enhancement. These findings indicate that the *cis*-enhancer function of the CNS13 fragment is dependent on these binding sequences.

We then examined binding of MEF2 and AP1 protein to CNS13. As demonstrated by the electrophoretic mobility shift assay (EMSA) outlined in *Figure 3A*, a slow-migrating band was visualized as a result of interaction between the CNS13 probe and the myc-tagged AP1 protein (lane 2). Another complex was also formed when myc-tagged MEF2 protein was co-incubated with the CNS13 probe (lane 4). Myc-antibody also formed additional complexes (lanes 3 and 5). To precisely identify the DNA sequences recognized by MEF2 and AP1 proteins, we performed competitive EMSA using unlabelled competitors composed of partial CNS13 sequences. As shown in *Figrue 3B*, the signal for the CNS13–AP1 complex was attenuated by the addition of AP1 competitor (lane 4), but not MEF2 competitor (lane 3), indicating that the complex formation is AP1-sequence specific. In CNS13–MEF2 complex competition assays, the opposite patterns were observed (*Figure 3C*). In addition, we amplified a genomic DNA fragment of CNS13 using ChIP with antibodies directed against AP1 and MEF2 (*Figure 3D*). These findings strongly suggest that MEF2 and AP1 transcription factors bind to CNS13 and play an important physiological role in *Hcn4* transcription.

3.3 dnMEF2 resulted in reduced Hcn4 expression

Among the MEF2 family of transcription factors, *MEF2A*, *C*, and *D* are expressed in cardiomyocytes.[10] Given that AP1 is a ubiquitously expressed transcription factor, we focused our study on the physiological role of MEF2. It has previously been shown that MEF2 proteins form hetero- and homodimers and that overexpression of dnMEF2 inhibit its transcriptional activity.[11] The schematic in *Figure 4A* outlines the structure of dnMEF2. In the current study, we demonstrate that dnMEF2 significantly reduced the transcriptional activity of the luciferase reporter vectors and that the enhancer activity of CNS13 was attenuated to 12% of the control levels. When MEF2 binding motif of CNS13 was disrupted, the overexpression of dnMEF2 did not significantly inhibit the enhancer activity (*Figure 4B*).

In order to examine the physiological role of *MEF2 in vivo*, we next expressed dnMEF2 using the AAV1 vector in cardiomyocytes isolated from the inflow tract of the embryonic rat heart, a site in which the HCN4 channel is highly

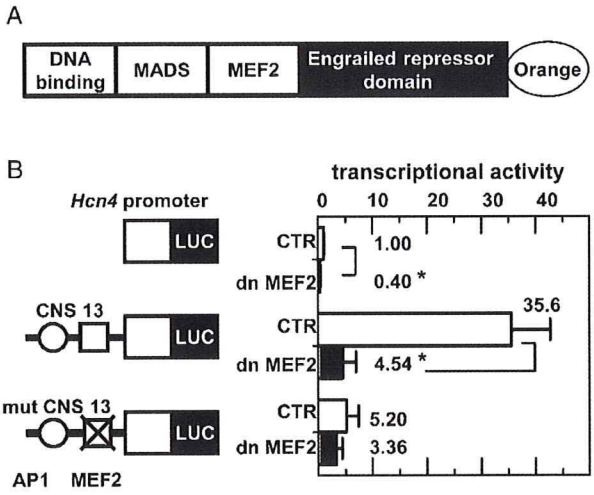

Figure 4 dnMEF2 inhibits *Hcn4* enhancer activity. (*A*) A schematic of the structure of dominant negative MEF2 mutant originated from MEF2C. (*B*) Transcriptional activity of the *Hcn4* promoter and CNS13, but not MEF2 site mutated CNS13, are significantly suppressed by dnMEF2. Along with luciferase reporter constructs, pAAV-dnMEF2 (0.3 μg) or pAAV-GFP (control; 0.3 μg) plasmids were cotransfected. Data are presented as relative values to the activity of the *Hcn4* promoter ($n = 4$; $^*P < 0.05$).

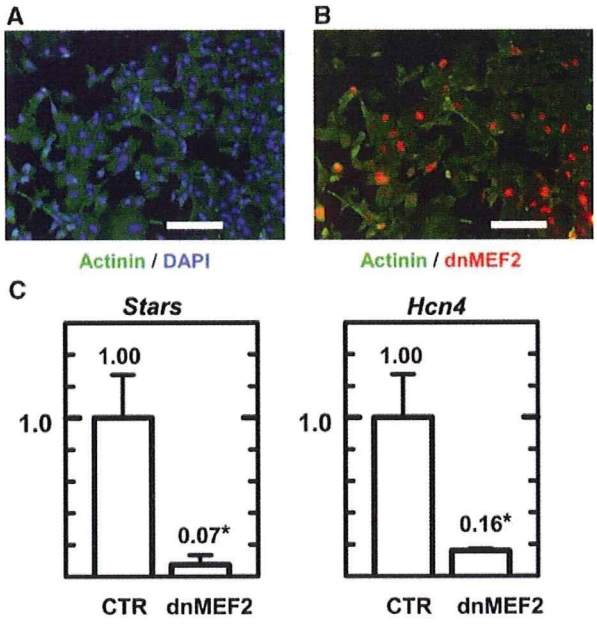

Figure 5 AAV1-dnMEF2 resulted in a reduction in *Stars* and *Hcn4* mRNA levels. (*A*) Immunofluorescent staining of cardiomyocytes for actinin (green). Nucleus is counter stained with DAPI (blue). Approximately 99% of the cells are actinin positive. Bar, 100 μm. (*B*) AAV1-dnMEF2 transfected myocytes demonstrate a nuclear orange fluorescent signal. Approximately 70% of the cells are transfected. (*C*) Relative mRNA levels measured by Q-PCR. Left, *Stars*. Right, *Hcn4*. ($n = 4$; $^*P < 0.05$ vs. control).

expressed.[12] As shown in *Figure 5A*, ~70% of cardiomyocytes was successfully transfected with dnMEF2. Three days following the transfection, *Hcn4* expression levels of Hcn4 were evaluated using real-time PCR. We also evaluated the expression levels of striated muscle activator of Rho signalling (*Stars*), which is known as a direct transcriptional target of MEF2.[13] As shown in *Figure 5A* and *B*, we found

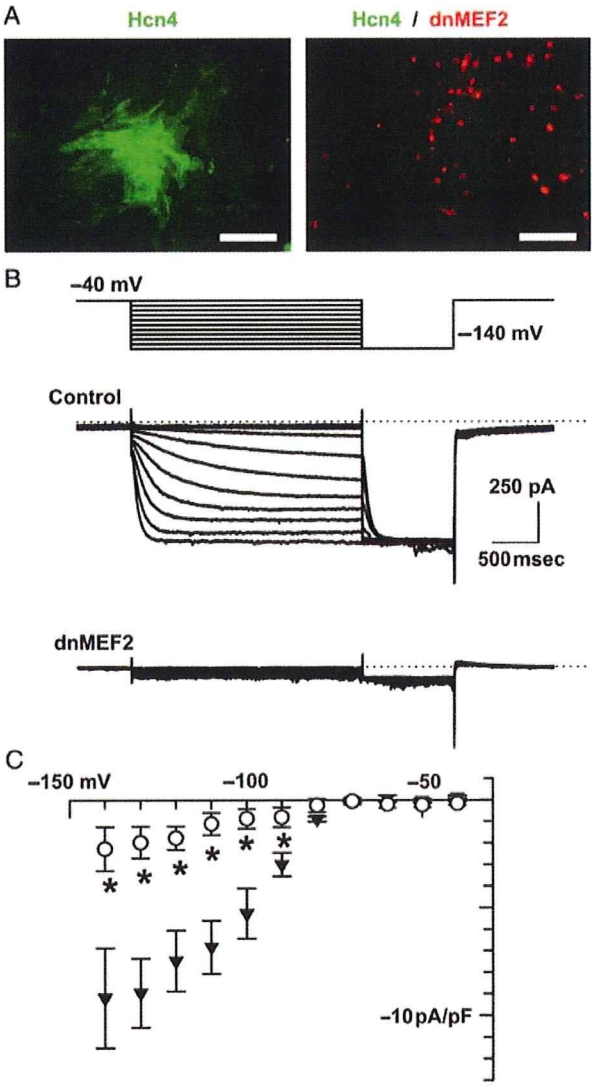

Figure 6 AAV1-dnMEF2 suppressed functional expression of the HCN4 channel. (*A*) Immunostaining for HCN4 (green). Left, control. Right, AAV1-dnMEF2. Bar, 100 μm. (*B*) I_h recorded in embryonic myocytes. The pulse protocol is shown in the top panel. The dotted line indicates the zero current level. (*C*) Current–voltage diagram of I_h. The amplitude of time-dependent current elicited by hyperpolarization was normalized by cellular capacitance. Filled triangle, control; open circle, dnMEF2 ($n = 7$; $^*P < 0.05$).

that both *Stars* and *Hcn4* mRNA levels were significantly reduced in dnMEF2-transfected myocytes, when compared with GFP-transfected myocytes as the negative control. In dnMEF2-transfected myocytes, however, the mRNA levels of HCN1 and HCN2, other types of HCN channels expressed in the heart, were not changed significantly (Supplementary material online, *Figure S1*). These channels might be regulated by different transcriptional mechanisms.[14]

We finally examined the functional expression of the HCN4 channel in embryonic myocytes transfected with dnMEF2. As shown in *Figure 6A* (left panel), HCN4 protein was clearly identified in control myocytes. However, only faint staining of HCN4 protein was observed in the myocytes transfected with dnMEF2 (nuclear-localized orange signals). In accordance with this, robust I_h current was also recorded in the control myocytes (*Figure 6B*, upper traces), whereas I_h

current was significantly reduced in dnMEF2-transfected myocytes (*Figure 6B*, lower traces). *Figure 6C* outlines the current–voltage diagram. The amplitude of I_h in dnMEF2-transfected myocytes was ~18% of the control myocytes. Similar results were also obtained for ES-derived cardiomyocytes (data not shown).[15]

4. Discussion

The transcription factors AP1 and MEF2 are known to play a variety of roles in the development of the heart. It has been reported that the ablation of *c-jun*, who along with *c-fos* forms the AP1 transcription factor, gave rise to the anomalies of right ventricular outflow tract and a reduction in *Cx43* expression.[16] Although we did not examine the direct physiological role of AP1 in the present study, it appears reasonable to expect that the expression of the *Hcn4* gene might also be reduced following the deletion of the AP1 protein. During development, *MEF2C* is known to be the predominant form of *MEF2* expressed in the embryonic heart. *MEF2A* and *MEF2D* became the major *MEF2* forms after birth.[10] Gene knockout of *MEF2C* results in an embryonic lethal phenotype.[17] MEF2D$^{-/-}$ mice are viable, demonstrating a weak response to hypertrophic stimulation.[18] *MEF2A* knockout mice generated on a 129Sv background die immediately following birth and demonstrate sinus arrhythmia and conduction block.[19] As the present study demonstrates that the expression of *Hcn4* is dependent on MEF2, it would be interesting to explore the ion channel expression in SAN of *MEF2A*$^{-/-}$ animals.

Recent studies have suggested that the *Nkx2-5* and *Pitx2c* transcription factors repress the expression of *Hcn4* in chamber myocardium, a result that is likely due to the inhibition of activators.[16] However, activators of *Hcn4* have not been identified in cardiomyocytes to date. The results of the current study suggest that MEF2 and AP1 may be candidate activators. The transcription factor *Tbx3*, in addition to *Hcn4*, is also specifically expressed in SAN. Ectopic expression of *Tbx3* in the atrium is known to induce *Hcn4* expression. However, it remains unclear whether *Hcn4* is a direct target of *Tbx3*.[5] Interestingly, we identified conserved MEF2- and AP1-like sequences within the *tbx3* gene locus. The spatiotemporal expression of *Tbx3* and *Hcn4* might be regulated via similar mechanisms.

MEF2 expression in the heart has been shown to be increased in the atrium.[20] Therefore, regional differences in *MEF2* expression might account in part for the spatial distribution of *Hcn4*. In this respect, it appears to be particularly important to investigate whether CNS13 is able to reproduce the spatiotemporal expression pattern of *Hcn4* in the heart. Although we have generated transgenic mice harbouring a *LacZ* reporter gene driven by the CNS13 and *Hcn4* promoter, we were unable to obtain consistent patterns of β-gal expression in embryos (data not shown). Thus, it is speculated that a combination of multiple CNSs may be required to reproduce the precise spatiotemporal expression pattern of *Hcn4*. Future studies will be required to address this question.

Supplementary material

Supplementary Material is available at *Cardiovascular Research* online.

Acknowledgements

We thank Dr M.A. Arnold for providing the dominant negative MEF2 cDNA.

Conflict of interest: none declared.

Funding

This work was supported in part by a Grant from the Vehicle Racing Commemorative Foundation and a Grant-in-Aid for Scientific Research from JSPS (#20300141).

References

1. Shram G, Pourrier M, Melnyk P, Nattel S. Differential distribution of cardiac ion channel expression as a basis for regional specialization in electrical function. *Circ Res* 2002;**90**:939–950.
2. Marionneau C, Couette B, Liu J, Mangoni M-E, Nargeot J, Lei M *et al.* Specific pattern of ion channel gene expression associated with pacemaker activity in the mouse heart. *J Physiol* 2005;**562**:223–234.
3. Ishii TM, Takano M, Xie L-H, Noma A, Ohmori H. Molecular characterization of the hyperpolarization-activated cation channel in rabbit heart sinoatrial node. *J Biol Chem* 1999;**274**:12835–12839.
4. Hermann S, Stieber J, Ludwig A. Pathophysiology of HCN channels. *Pflügers Arch* 2007;**454**:517–522.
5. Hoogaars W-M, Engel A, Brons J-F, Verkerk A-O, de Lange F-J, Wong L-Y *et al.* Tbx3 controls the sinoatrial node gene program and imposes pacemaker function on the atria. *Genes Dev* 2007;**21**:1098–1112.
6. Mommersteeg M-T, Hoogaars W-M, Prall O-W, de Gier-de Vries C, Wiese C, Clout D-E *et al.* Molecular pathway for the localized formation of the sinoatrial node. *Circ Res* 2007;**100**:354–362.
7. Pennacchio L-A, Ahituv N, Moses A-M, Prabhakar S, Nobrega M-A, Shoukry M *et al. In vivo* enhancer analysis of human conserved non-coding sequences. *Nature* 2006;**444**:499–502.
8. Visel A, Minovitsky S, Dubchak I, Pennacchio L-A. VISTA Enhancer Browser—a database of tissue-specific human enhancers. *Nucleic Acids Res* 2007;**35**:D88–D92.
9. Kuratomi S, Kuratomi A, Kuwahara K, Ishii TM, Nakao K, Saito Y *et al.* NRSF regulates the developmental and hypertrophic changes of HCN4 transcription in rat cardiac myocytes. *Biochem Biophys Res Commun* 2007;**353**:67–73.
10. Potthoff M-J, Olson E-N. MEF2: a central regulator of diverse developmental programs. *Development* 2007;**134**:4131–4140.
11. Arnold M-A, Kim Y, Czubryt M-P, Phan D, McAnlly J, Qi X *et al.* MEF2C transcription factor controls chondrocyte hypertrophy and bone development. *Dev Cell* 2007;**12**:377–389.
12. Li X-G, Okada T, Kodera M, Nara Y, Takino N, Muramatsu C *et al.* Viral-mediated temporally controlled dopamine production in a rat model of Parkinson disease. *Mol Ther* 2006;**13**:160–166.
13. Kuwahara K, Teg Pipes G-C, McAnally J, Richardson J-A, Hill J-A, Bassel-Duby R *et al.* Modulation of adverse cardiac remodeling by STARS, a mediator of MEF2 signaling and SRF activity. *J Clin Invest* 2007;**117**:1324–1334.
14. Pachucki J, Burmeister LA, Larsen PR. Thyroid hormone regulates hyperpolarization-activated cyclic nucleotide-gated channel (HCN2) mRNA in the rat heart. *Circ Res* 1999;**85**:498–503.
15. Yanagi K, Takano M, Narazaki G, Uosaki H, Hoshino T, Ishii T *et al.* HCN and Cav3 channels confer automaticity of embryonic stem-derived cardiomyocytes. *Stem Cells* 2007;**25**:2712–2719.
16. Jochum W, Passegue E, Wagner EF. AP-1 in mouse development and tumorigenesis. *Oncogene* 2001;**20**:2401–2412.
17. Lin Q, Schwarz J, Bucana C, Olson E-N. Control of mouse cardiac morphogenesis and myogenesis by transcription factor MEF2C. *Science* 1997;**276**:1404–1407.
18. Kim Y, Phan D, vanRooij E, Wang D-Z, McAnally J, Qi X *et al.* The MEF2D transcription factor mediates stress-dependent cardiac remodeling in mice. *J Clin Invest* 2008;**118**:124–132.
19. Naya F-J, Black B-L, Wu H, Bassel-Duby R, Richardson J-A, Hill J-A *et al.* Mitochondrial deficiency and cardiac sudden death in mice lacking MEF2A transcription factor. *Nat Med* 2002;**11**:1303–1309.
20. Zhao X-S, Gallardo T-D, Lin L, Schageman J-J, Shohet R-V. Transcriptional mapping and genomic analysis of the cardiac atria and ventricles. *Physiol Genomics* 2002;**12**:53–60.

SYNAPSE 63:541–548 (2009)

Multitracer Assessment of Dopamine Function After Transplantation of Embryonic Stem Cell-Derived Neural Stem Cells in a Primate Model of Parkinson's Disease

SHIN-ICHI MURAMATSU,[1]* TSUYOSHI OKUNO,[2] YUTAKA SUZUKI,[2] TAKASHI NAKAYAMA,[3] TAKEHARU KAKIUCHI,[4] NAOMI TAKINO,[1] ASAKO IIDA,[1] FUMIKO ONO,[5] KEIJI TERAO,[5] NOBUO INOUE,[6] IMAHARU NAKANO,[1] YASUSHI KONDO,[2] AND HIDEO TSUKADA[4]

[1]*Divison of Neurology, Department of Medicine, Jichi Medical University, Tochigi 329-0498, Japan*
[2]*Mitsubishi Tanabe Pharma Corporation, Osaka 532-8505, Japan*
[3]*Department of Biochemistry I, Yokohama City University School of Medicine, Kanagawa 236-0004, Japan*
[4]*Central Research Laboratory, Hamamatsu Photonics K.K., Shizuoka 434-8601, Japan*
[5]*Tsukuba Primate Research Center, National Institute of Biomedical Innovation, Ibaraki 305-0843, Japan*
[6]*Division of Regenerative Neurosciences, Tokyo Metropolitan University, Tokyo 116-8551, Japan*

KEY WORDS ES cell; PET; monkey; MPTP

ABSTRACT The ability of primate embryonic stem (ES) cells to differentiate into dopamine (DA)-synthesizing neurons has raised hopes of creating novel cell therapies for Parkinson's disease (PD). As the primary purpose of cell transplantation in PD is restoration of dopaminergic neurotransmission in the striatum, in vivo assessment of DA function after grafting is necessary to achieve better therapeutic effects. A chronic model of PD was produced in two cynomolgus monkeys (M-1 and M-2) by systemic administration of neurotoxin. Neural stem cells (NSCs) derived from cynomolgus ES cells were implanted unilaterally in the putamen. To evaluate DA-specific functions, we used multiple [^{11}C]-labeled positron emission tomography (PET) tracers, including [β-^{11}C]L-3,4-dihydroxyphenylalanine (L-[β-^{11}C]DOPA, DA precursor ligand), [^{11}C]-2β-carbomethoxy-3β-(4-fluorophenyl)tropane ([^{11}C]β-CFT, DA transporter ligand) and [^{11}C]raclopride (D_2 receptor ligand). At 12 weeks after grafting NSCs, PET demonstrated significantly increased uptake of L-[β-^{11}C]DOPA (M-1:41%, M-2:61%) and [^{11}C]β-CFT (M-1:31%, M-2:36%) uptake in the grafted putamen. In addition, methamphetamine challenge in M-2 induced reduced [^{11}C]raclopride binding (16%) in the transplanted putamen, suggesting release of DA. These results show that transplantation of NSCs derived from cynomolgus monkey ES cells can restore DA function in the putamen of a primate model of PD. PET with multitracers is useful for functional studies in developing cell-based therapies against PD. **Synapse 63:541–548, 2009.** ©2009 Wiley-Liss, Inc.

INTRODUCTION

In Parkinson's disease (PD), the cardinal symptoms such as rest tremor, muscular rigidity and bradykinesia, become apparent after 40–50% of the neurons in the substantia nigra pars compacta (SNc) have been lost and striatal dopamine (DA) has been reduced to about 20% of normal levels (Kish et al., 1988). As a treatment for advanced PD, neural transplantation has been investigated for more than two decades with the aim of replacing degenerated DA neurons and restoring dopaminergic neurotransmission in the striatum. Embryonic stem (ES) cells may offer a substitute for currently used fetal midbrain cells, because they can proliferate extensively in an undifferentiated state and may provide an unlimited source of DA neurons (Li et al., 2008; Newman and Bakay, 2008). Transplantation of DA neurons derived from mouse ES cells

Contract grant sponsors: Ministry of Health, Labor and Welfare of Japan, Ministry of Education, Culture, Sports, Science and Technology of Japan (Special Coordination Funds), Japan Society for the Promotion of Science (Grant-in-Aid for Creative Scientific Research), CREST, the Japan Science and Technology Agency (JST).

*Correspondence to: Shin-Ichi Muramatsu, Division of Neurology, Department of Medicine, Jichi Medical University, 3311-1 Yakushiji, Shimotsuke, Tochigi 329-0498, Japan. E-mail: muramats@ms.jichi.ac.jp

Received 18 August 2008; Accepted 31 October 2008

DOI 10.1002/syn.20634

Published online in Wiley InterScience (www.interscience.wiley.com).